

# **A Thermophotovoltaic Catalytic Flow Reactor for Portable Power Generation**

A thesis submitted by

Abigail S. Licht

In partial fulfillment of the requirements for the degree of

Master of Sciences

in

Electrical Engineering

TUFTS UNIVERSITY

August 2015

Thesis Adviser: Professor Thomas Vandervele

Committee: Professor Marc Hodes and Professor Ronald Lasser

## **ABSTRACT**

Although batteries are the standard technology for portable power generation, they have relatively low energy densities: on average 0.2 kWhr/kg. Hydrocarbons, on the other hand, can have energy densities as high as 12 kWhr/kg, such that even an inefficient fuel-powered portable generator could surpass the performance of state of the art batteries. Moreover, while some of the most energy-dense batteries are non-rechargeable, simply refueling can quickly recharge a hydrocarbon-powered supply. Traditional heat engines, however, do not scale well: micro-heat engines are plagued with friction losses due to moving parts. The larger surface-area-to-volume ratio also leads to increased heat losses, which prevent a sustained reaction from occurring. A promising alternative for small-scale portable power applications incorporates Thermophotovoltaics (TPV) in place of a heat engine. Instead of converting the heat to mechanical energy, the heat is directly converted to electricity through traditional photovoltaic mechanisms. Unlike micro-engines, TPVs are structurally simple and have no moving parts. A propane-fueled TPV generator could significantly extend the “battery lifetime” of portable electronic devices. Consumer, military, medical, and remote sensing devices would benefit from developments in this field.

Here, we design and implement a combustion system that will supply radiant energy to TPV. This project is twofold: First, there is the design and

testing of a novel meso-scale combustion system. Propane fuel is catalytically combusted by a platinum-plated nickel foam insert. With a fuel to air equivalence ratio of  $\Phi = 0.83$ , a combustion efficiency of 7.4% is achieved. Second, we investigate methods for extending the operational wavelengths of TPV devices, which are needed to optimally convert the meso-combustor emission spectrum. We employ a superlattice barrier structure to suppress diffusion currents, decreasing dark current and improving overall power characteristics. Through simulation with Silvaco software we find that the barrier structure improves the relative diode efficiency by 26.5%. Finally, we investigate the limit for longer wavelength devices based doping-restraints and intrinsic carrier concentrations for room-temperature operation.

## ACKNOWLEDGEMENTS

*First and foremost, I would like to express my sincere gratitude to my adviser Professor Tom Vandervelde for his extraordinary mentorship. I am incredibly grateful to have the opportunity to work with you and learn from you every day.*

*In addition to my adviser, I would also like to thank Professor Marc Hodes and Professor Ronald Lasser for serving on my thesis committee; I greatly appreciate your invaluable feedback and expertise.*

*I would also like to note and thank our collaborators: Dr. Jean Baptiste Rodriguez from the University of Montpellier for working with us on the MBE growth of the superlattice materials and Dr. Jay Peck for providing the original catalyst recipe for the combustor.*

*Special thanks to my fellow and former lab mates: Dante DeMeo for pioneering this project and also Nicole, Maggie, Ahmed, John, Chandler, and Corey.*

*Last, but certainly not least, I would like to thank my family and friends. Mom, Dad, Anna, Jacob, Dan, and Emma: I am infinitely grateful for your love and support. Thank you.*

# TABLE OF CONTENTS

<b>ABSTRACT .....</b>	<b>2</b>
<b>ACKNOWLEDGEMENTS .....</b>	<b>4</b>
<b>TABLE OF CONTENTS .....</b>	<b>5</b>
<b>LIST OF FIGURES .....</b>	<b>8</b>
<b>LIST OF TABLES .....</b>	<b>12</b>
<b>1 INTRODUCTION .....</b>	<b>13</b>
1.1 MOTIVATION .....	13
1.2 A THERMOPHOTOVOLTAIC CATALYTIC FLOW REACTOR (TPV-CFR) .....	14
1.3 COMPETING FUEL-BASED PORTABLE POWER TECHNOLOGIES.....	15
1.3.1 <i>Fuel Cells</i> .....	15
1.3.2 <i>Heat Engines</i> .....	17
1.3.3 <i>Thermoelectric Generators</i> .....	18
1.3.4 <i>Comparison of Technologies</i> .....	20
1.4 THESIS ORGANIZATION .....	21
<b>2 MICROCOMBUSTOR .....</b>	<b>22</b>
2.1 PREVIOUS WORK: COMBUSTION PORTABLE POWER SYSTEMS WITH TPV ...	22
2.1.1 <i>Macro-Scale Burners</i> .....	22
2.1.2 <i>Micro-Scale Burners</i> .....	24
2.2 OUR APPROACH .....	27
2.3 DESIGN DETAILS .....	27
2.3.1 <i>Catalytic Flow Reactor</i> .....	27
2.3.2 <i>Fuel Choice</i> .....	30
2.4 EXPERIMENT AND RESULTS.....	30

2.4.1	<i>Power Goal and Flow Rates</i>	30
2.4.2	<i>Adiabatic Flame Temperature</i>	31
2.4.3	<i>Ignition</i>	31
2.4.4	<i>Combustion Efficiency</i>	32
2.4.5	<i>Results</i>	34
2.5	CHAPTER SUMMARY	38
<b>3</b>	<b>THERMOPHOTOVOLTAICS</b>	<b>40</b>
3.1	INTRODUCTION	40
3.2	PHOTOVOLTAIC BACKGROUND	40
3.2.1	<i>Conductors, Semiconductors, and Insulators</i>	40
3.2.2	<i>Doping</i>	42
3.2.3	<i>The PN Junction</i>	44
3.2.4	<i>The Ideal Diode Current</i>	46
3.2.5	<i>Deviations from Ideality: The RG Current</i>	49
3.2.6	<i>Photodiode operation</i>	54
3.2.7	<i>PV Circuit Model</i>	56
3.3	TPV DIODE MATERIALS	58
3.4	EXTENDING THE OPERATIONAL WAVELENGTH OF TPV	60
3.4.1	<i>Optimal Bandgap for Emitter Temperature</i>	61
3.4.2	<i>Decreasing recombination/reducing dark current for TPV</i>	64
3.4.3	<i>Simulations</i>	70
3.4.4	<i>Growth, Characterization, and Processing</i>	83
3.5	CHAPTER SUMMARY	85
<b>4</b>	<b>SYSTEM EFFICIENCY</b>	<b>87</b>
4.1	SYSTEM EFFICIENCY CALCULATIONS	87
4.1.1	<i>Chemical to Radiation Efficiency</i>	87

4.1.2	<i>View Factor</i> .....	88
4.1.3	<i>TPV Cell Conversion Efficiency</i> .....	88
4.1.4	<i>Total System Efficiency</i> .....	89
4.2	IMPROVING SYSTEM EFFICIENCY.....	90
4.2.1	<i>Stabilizing the Combustion Reaction and Reducing Heat Losses</i> ....	90
4.2.2	<i>Incorporating Spectral Control</i> .....	92
4.2.3	<i>Improving TPV Cell Efficiency</i> .....	93
4.3	CHAPTER SUMMARY.....	94
<b>5</b>	<b>THESIS SUMMARY</b> .....	<b>95</b>
	<b>APPENDIX</b> .....	<b>99</b>
A.	CATALYST RECIPE.....	99
B.	MASS FLOW RATE CALCULATIONS.....	100
	<b>REFERENCES</b> .....	<b>101</b>

## LIST OF FIGURES

Figure 1-1: Comparison of the specific energy of various power sources [1].	14
Figure 1-2: Overview of TPV-CFR. In the first stage, fuel and air are fed to the reactor and catalytically combusted. In the second stage, the TPV cell converts the infrared radiation from the heated emitter into electricity.	15
Figure 1-3: Proton exchange membrane fuel cell.	16
Figure 1-4: Thermoelectric Generator	19
Figure 2-1: Original TPV Design [8].	23
Figure 2-2: JX Crystal TPV battery with fuel cylinder 2011 Design [9]	24
Figure 2-3: Temperature vs. power supplied [12]	26
Figure 2-4: Combustion chamber and gasket: The chamber consists of three plates which	28
Figure 2-5: The spectral emissivity of SiC at varying high temperatures. SiC has a high emissivity at the desirable wavelengths ( $<1.74\mu\text{m}$ ). [21]	29
Figure 2-6: Exploded view of chamber: The catalyst (green) sits inside the chamber. Three cell holder plates can hold up to nine TPV cells (yellow). A cooling chamber keeps the TPV cells at low temperatures.	29
Figure 2-7: Combustion results: combustion was indicated by a $263^{\circ}\text{C}$ jump in temperature of the catalyst over the course of five seconds.	34
Figure 2-8: Catalyst post-combustion testing: blackened marks indicate combustion only occurred on one side of catalyst.	35
Figure 2-9: XPS spectrum of the etched catalyst surface. The sharp peak at $\sim 100\text{eV}$ indicates a high concentration of platinum.	36
Figure 3-1: Band diagram representation for conductors, semiconductors, and insulators.	41
Figure 3-2: N-type (left) and p-type (right) band structures. In an n-type material, the high doping of donor atoms shifts the Fermi level upward. In a p-type material, the high doping of acceptor atoms shifts the Fermi level downward.	43
Figure 3-3: i. Isolated n-type and p-type materials ii. Electrons from the n-type material diffuse into the p-type material, recombining with holes; holes from	

the p-type material diffuse into the n-type material, recombining with electrons iii. Positive ions are uncovered in the n-type region; negative ions are uncovered in the p-type region. An electric field is set up between the two depleted regions.....44

Figure 3-4: Band diagrams for isolated n-type and p-type materials (top) and the heterojunction pn diode (bottom). For the n-type material, the Fermi level is close to the conduction band edge. For the p-type material, the Fermi level is close to the valence band edge. The Fermi level remains constant for any material under zero bias; thus, when the p and n materials are combined to form a heterojunction, band bending occurs. The built-in potential and electric field occur throughout the band-bending region.....45

Figure 3-5: Visualization of drift and diffusion currents. Electrons are represented by solid circles and holes are represented by open circles. Minority carriers, which result in a drift current, are shown in blue. Majority carriers, which result in diffusion current, are shown in green. At zero applied bias, these two currents cancel each other exactly.....47

Figure 3-6: Diode currents in reverse bias. Electrons are represented by solid circles and holes are represented by open circles. Minority carriers, which result in a drift current, are shown in blue. The high barrier in reverse bias blocks majority carriers. ....47

Figure 3-7: Diode current mechanism in forward bias. Electrons are represented by solid circles and holes are represented by open circles. Minority carriers, which result in a drift current, are shown in blue. The barrier height decreases with increasing applied forward bias, and the diffusion current due to the majority carrier injection increase exponentially. ....48

Figure 3-8: Current-Voltage curve for ideal diode. For reverse bias, the diode quickly approaches the saturation current. For forward biases, the current increases exponentially with increasing voltage. ....49

Figure 3-9: Plot of diode current versus temperature. Diffusion current is the dominant current for high temperatures and generation-recombination current is the dominant current for low temperatures. The crossover temperature is designated by  $T_0$ . ....53

Figure 3-10: Current-voltage characteristic of an ideal diode in dark (blue curve) and light (red curve). ....55

Figure 3-11: Circuit diagram for photovoltaic cell including series and shunt resistances.....57

Figure 3-12: Sub-section of the periodic table showing the group III and V elements that are incorporated into TPV diode materials.....59

Figure 3-13: Plot of the power density of various bandgap TPV cells as a function of temperature. The shorter bandgap diodes have a higher power density. For example, the 0.25eV cell has a power density of 6.5 W/cm<sup>2</sup> at 1,000°C whereas the 1.1eV bandgap diode has a power density of only 0.06 W/cm<sup>2</sup> at 1,000°C.....63

Figure 3-14: The conduction band (red) and valance band (blue) are represented by solid lines and electron and hole minibands are represented by dashed lines. There are three possible band alignments. T1SL has material A with lower conduction band and higher valence band than material B. For T2SL, both the conduction band and valence band of A are lower than that of B – confining electrons and holes to separate materials. T2SL is further classified based on the relative alignment of the conduction band of material A and the valence band of material B. If the conduction band of A is higher than the valence band of B, than the material is type-IIA. If the conduction band of A is lower than the valence band of B, then the material is classified as type-IIB.....65

Figure 3-15: Dark-field image of a 50 period InAs/GaSb superlattice [45] .....66

Figure 3-16: T2SL InAs/GaSb band alignment: The conduction band is shown in red and the valence band is shown in blue. The effective bandgap is the difference in energy of the electron and hole minibands, created from the overlapping wave functions of the constituent materials. ....67

Figure 3-17: Bariode band diagram. For a monovalent barrier, minority carrier and majority carrier holes are blocked, which contribute to the dark current. Photogenerated carriers are not blocked.....69

Figure 3-18: Plot comparing dark current values for two diodes. The diode with the lower saturation current is shown in red. The decreased saturation current leads to a higher turn on voltage. ....70

Figure 3-19: SEPM results. Contour lines are plotted for constant conduction band versus constant bandgap. The point (10 ML InAs, 13 ML GaSb) occurs at 0.24eV. A line of constant conduction band is traced to the point (5 ML InAs, 4 ML GaSb) at 0.35eV to ensure that the change in band is entirely over the valence band.....72

Figure 3-20: Intrinsic carrier concentration versus cut-off wavelength for room temperature operation. The regions are color-coded to correspond to acceptable doping concentrations (yellow), trade-off doping concentrations (orange), and unacceptable doping concentrations (red) .....76

Figure 3-21: Band diagram for InAs/GaSb pin (top) and nBp (bottom) structures (p-region truncated for ease of viewing). The bandgap of the n-layer is 0.248 eV and the bandgap of the p-type absorber is 0.24 eV; the barrier has a bandgap of 0.35 eV resulting in a barrier of 100 meV to thermally generated holes from the n-region. The structures both have a 1300nm thick absorption region. The doping for the n-region and the p-region is  $1 \times 10^{18} / \text{cm}^3$  and  $5 \times 10^{18} / \text{cm}^3$ , respectively. ....77

Figure 3-22: Diode stack: The diode is 1.805 microns thick. The intrinsic/barrier region is shown in orange and the p-type absorber region is shown in blue. The n-layer is very thin and is not visible here. The contact is also not visible here: the top contact covers 10% of the surface area. ....78

Figure 3-23: Plot of diffusion current versus voltage for pin (black) and pBn (green) for  $N_a=5 \times 10^{18}$  and  $N_D=1 \times 10^{18}$  at room temperature. For a 5  $\mu\text{m}$  cut-off wavelength InAs/GaSb SL photodiode, the pBn diffusion current is reduced by a factor of  $\sim 300$  as compared to the pin diffusion current. ....79

Figure 3-24: Plot of dark current as simulated with Silvaco at 300K showing the reduction in dark current for the pBn over the pin structure. ....80

Figure 3-25: Plot of open-circuit voltage versus temperature for the pBn and pin devices. As the temperature increases, the open-circuit voltage of both devices decreases, but the pBn maintains a higher open-circuit voltage as compared to the pin. ....81

Figure 3-26: Current-voltage curve for pin and pBn under illumination by a 1000°C blackbody spectrum and room temperature operation. ....82

Figure 3-27: Simulated internal and external quantum efficiency of 5  $\mu\text{m}$  TPV photodiode. ....83

Figure 4-1: Incident spectrum (blue), converted spectrum (green), and quantum efficiency (red) .....89

## LIST OF TABLES

Table 1-1: Comparison of fuel to electricity technologies for portable power generation. .....	20
Table 2-1: Elemental composition of surface treated samples before and after testing ..	37
Table 3-1: Bandgap and cutoff wavelength for optimal conversion efficiency for various emitter temperatures.....	62
Table 3-2: Doping levels and corresponding acceptable intrinsic carrier concentrations	75

# 1 Introduction

## 1.1 Motivation

Portable electronic devices are ubiquitous in our everyday lives, powering everything from radios to laptops. Typical power requirements for these devices range from 1-100 watts. Presently, the standard technology for powering these devices is the battery. However, despite being a mature technology, batteries have a relatively low energy density; the state-of-the-art rechargeable battery has not demonstrated an energy density greater than 1.2 MJ/kg. Hydrocarbon fuels, on the other hand, have energy densities as high as 120 MJ/kg [1]. The difference in energy density is depicted in Figure 1-1: here we see that the specific energy of hydrocarbon fuels is several orders of magnitude greater than the specific energy of batteries. By using fuel in place of batteries, then, a much lighter system can contain the same amount of energy. Similarly, for a system of the equivalent weight, more energy is available. This point was illustrated well by physicist Felix Weinberg:

*“I can put several million Joules safely into my pocket in the form of a large tin of lighter fuel. The cost of petroleum would have to rise several hundred times before the price of such a tin would be approximate to that of electrical storage batteries for a comparable amount of energy – and then they would be too heavy to pick up.” - Felix Weinberg [2]*

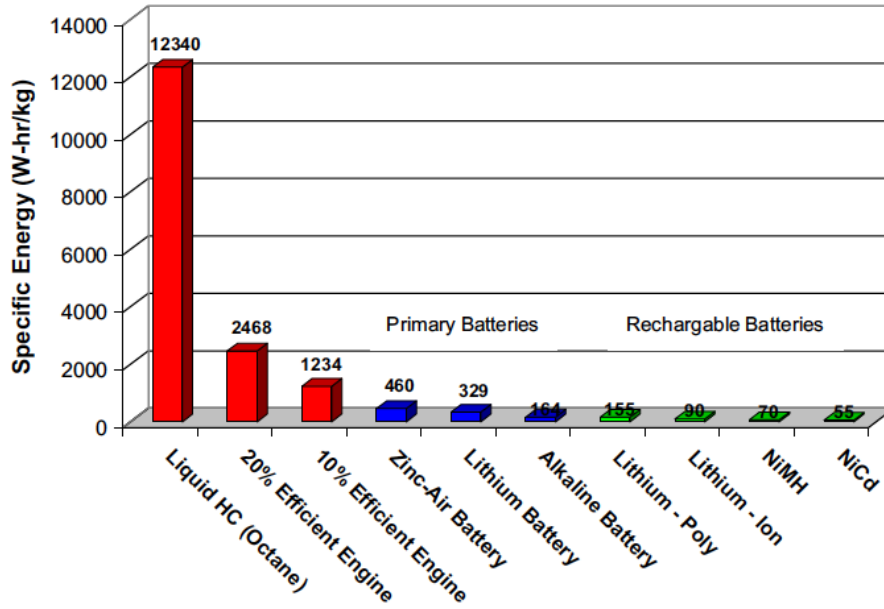


Figure 1-1: Comparison of the specific energy of various power sources [1].

In this thesis project, we seek to use the high specific energy of hydrocarbon fuels to generate an alternative portable power source. Our approach to this challenge is to create a thermophotovoltaic (TPV) catalytic flow reactor (CFR). An overview of this technology is provided in the following section. Competing technologies are then discussed and compared.

## 1.2 A Thermophotovoltaic Catalytic Flow Reactor (TPV-CFR)

A thermophotovoltaic (TPV) catalytic flow reactor (CFR) consists of two stages as depicted in Figure 1-2. In the CFR, a mixture of fuel and air is ignited catalytically in an exothermic reaction, generating heat. The energy released from the reactor is used in the second stage to heat an emitter, which radiates infrared photons towards a

thermophotovoltaic (TPV) cell. The TPV cell then absorbs the incident radiation, generating electron-hole pairs which are separated by the electric field of the TPV diode to produce a current. While this is one approach, several other fuel-to-electricity technologies have been investigated for portable power technologies and are detailed briefly in the next section.

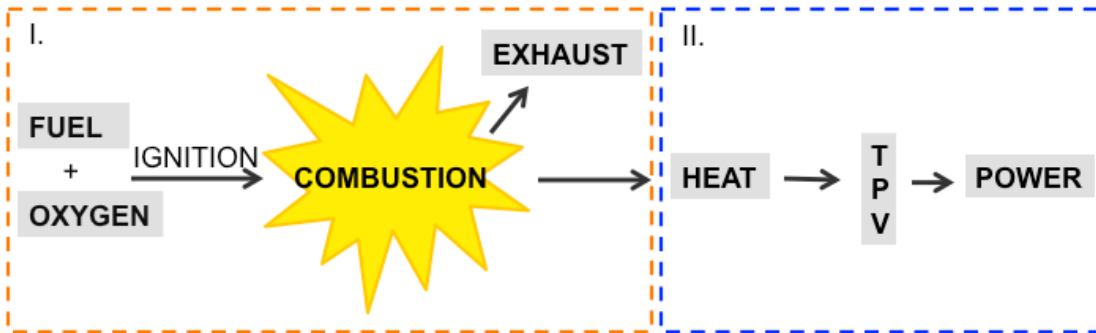


Figure 1-2: Overview of TPV-CFR. In the first stage, fuel and air are fed to the reactor and catalytically combusted. In the second stage, the TPV cell converts the infrared radiation from the heated emitter into electricity.

### 1.3 Competing Fuel-Based Portable Power Technologies

The energy from fuel may be used either directly (as in fuel cells) or indirectly (as with heat engines and thermoelectrics). Several competing methods are detailed below:

#### 1.3.1 Fuel Cells

A fuel cell converts chemical energy to electrical energy through a reduction-oxidation, or redox, reaction. The fuel cell consists of an anode and a cathode separated by an electrolyte material (Figure 1-3). A half reaction occurs at each

electrode, as shown in Equations 1.1 and 1.2, where  $Ox$  is the oxidized species,  $Re$  is the reduced species, and  $n$  is the number of electrons transferred. Oxidation occurs at the anode/electrolyte interface, where the fuel is oxidized (loss of electrons or increase in oxidation state), giving up an electron and forming a positive ion (Equation 1.1). The electrons at the anode are then drawn through an external circuit across the load and back through the cathode, transferring energy to the load. At the same time, the positively charged ions drift across the electrolyte where reduction (gain of electrons or decrease in oxidation state) occurs as the positive ions recombine with electrons and oxygen molecules at the cathode (Equation 1.2).

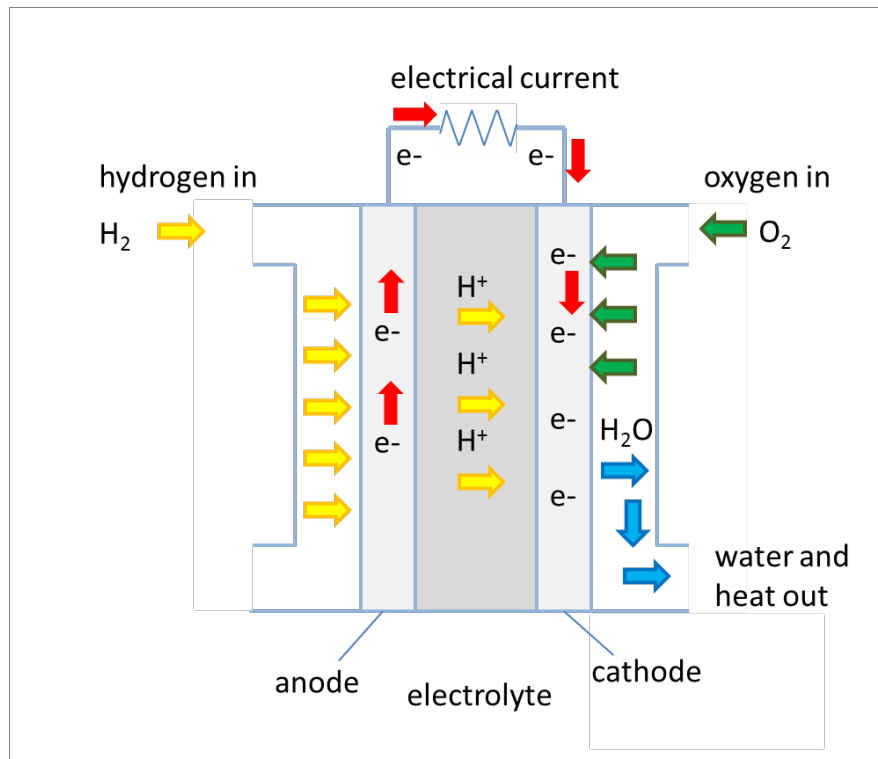


Figure 1-3: Proton exchange membrane fuel cell.

Advantages of using fuel cells for portable power systems include direct chemical-to-electrical energy conversion, high efficiencies (40-60%), and no moving parts [3]. Fuel cells, however, are not fuel-agnostic in their design; only certain fuels can be used with specified electrolyte materials. Moreover, scale down of fuel cells leads to complications, as it is difficult to produce thin film electrodes with a low activation polarization due to decreased active site area for the reaction. As a result, higher operating temperatures are required to overcome the activation barrier for thin film electrode fuel cells. This issue is considered the greatest hurdle to obtaining a decent power output for thin film electrode fuel cell technology [4].

Portable power fuel cell technology has advanced in the past few years and has been deployed to the U.S. Army by SFC Energy, a German manufacturer of direct methanol fuel cells. SFC has produced several models, with the most light-weight being the “Jenny ND Terra” model, which has a dry weight of 23.5 lbs. and a nominal power of 25 W [5]. This system is still relatively large, with dimensions of 19.7 by 15.5 by 9.5 inches. Moreover, while fuel cell technology is fairly mature, this system only offers a 50% improvement in weight over battery systems, whereas much higher ratios should be obtainable.

### **1.3.2 Heat Engines**

Fuel may also be converted to electricity via internal or external combustion engines, or “heat engines”, where chemical energy is converted to mechanical energy and subsequently to electrical energy. In an internal combustion engine, high-temperature high-pressure gases expand, applying force to a part of the engine, such as

a piston or turbine blade, converting chemical energy into mechanical energy. In an external combustion system, such as a steam engine, the energy from the gas is delivered to an intermediate working fluid, which then applies force to motional parts of the engine, transferring the energy to mechanical energy. In both cases, an electric generator may then be used to convert mechanical energy to electrical energy.

Conventional macro-scale heat engines have efficiencies of 25-60%. However, these engines do not scale down well: as the dimensions of the engine decrease, the surface-area-to-volume ratio increases, increasing both heat and frictional losses from the moving parts. Based on present technology limitations, micro-scale heat engines have foreseeable efficiencies of only 10-20% [4].

### 1.3.3 Thermoelectric Generators

Thermoelectrics (TE) convert heat into electricity via the Seebeck effect, in which an electrical potential is generated by a temperature difference across a material. Equation 1.3 gives the voltage which is equal to the product of the Seebeck coefficient ( $\alpha$ ) and the temperature difference ( $\Delta T$ ). While voltage is generated by the temperature difference, current flow is generating by incorporating both p-type (positively charged) and n-type (negatively charged) semiconductors. These p-type and n-type semiconductors are electrically in series but thermally in parallel, as can be seen in Figure 1-4.

$$V = \alpha \Delta T$$

1.3

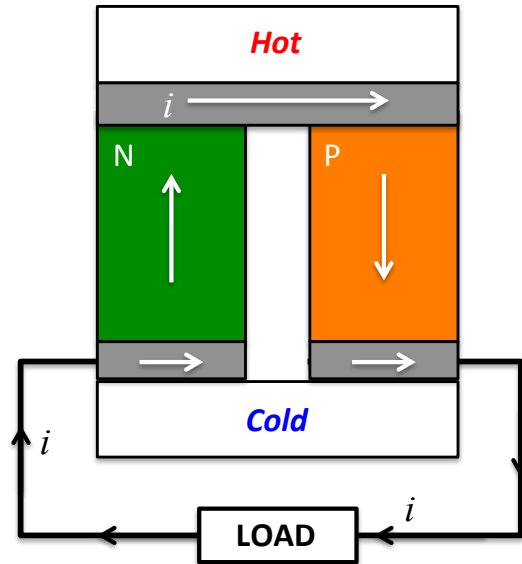


Figure 1-4: Thermoelectric Generator

The standard TE figure of merit is  $zT$ , Equation 1.4, and is proportional to the Seebeck coefficient ( $\alpha$ ) and temperature ( $T$ ) and inversely proportional to the electrical resistivity ( $\rho$ ) and thermal conductivity ( $\kappa$ ) of the material. Thermoelectrics are therefore optimized by maximizing electrical conductivity and minimizing thermal conductivity.

$$zT = \frac{\alpha T}{\rho \kappa} \quad 1.4$$

Bismuth Telluride ( $\text{Bi}_2\text{Te}$ ) TE materials have been incorporated into MEMS micro-burners, converting heat from propane and butane fuels. These TE systems, like fuel cells, have no moving parts. While thermoelectrics are less bulky than heat engines, they are more expensive and less efficient, achieving only 5-10%.

### 1.3.4 Comparison of Technologies

	Fuel Cells	Heat Engines	Thermoelectrics	TPV
Mechanically passive	✓	✗	✓	✓
Fuel flexibility	✗	✓	✓	✓
Low noise	✓	✗	✓	✓
Hot/cold separation	✗	✗	✗	✓
Modular fabrication	✗	✗	✗	✓

Table 1-1: Comparison of fuel to electricity technologies for portable power generation.

TPV paired combustion systems have several advantages over competing technologies (Table 1). Combustion is considered less complex and less limited in material choices than fuel cell chemistry. Moreover, unlike heat engines, TPVs have no moving parts, which reduces mechanical stresses and simplifies scale-down. Additionally, whereas for TE the hot and cold sides are in direct contact, for TPV, the energy converter is separated from the hot combustion process, thereby reducing thermal stresses for TPV.

Despite these advantages, efficiencies of small-scale combustion-driven TPV systems remain low and much work is required before this technology can reach commercialization. These systems are plagued by two major issues: for the combustion stage, increased surface-area-to-volume with scale down leads to major heat losses and

flame quenching; for the TPV stage, optimized TPV diodes with smaller bandgaps have yet to be developed. Further research and progress for both stages is necessary to enable this technology.

## **1.4 Thesis Organization**

The goal of this thesis is to develop a complete TPV-CFR system. The thesis has two main research thrusts. The first is the design and testing of a propane-fueled catalytic flow reactor. The second is the design of long wavelength thermophotovoltaic cells to optimally convert heat from the reactor into electrical energy. These long wavelength TPV diodes will also benefit other technologies, as they can be employed as a secondary energy source in heat recycling applications (for example, recycling waste heat from car exhaust).

In this chapter we presented motivation for a portable fuel-powered TPV generator. In the next chapter, the design and testing of a propane-fueled CFR is detailed. The following chapter describes the design and simulation of long wavelength TPV diodes to be used in conjunction with the CFR. The two stages are tied together in chapter four as we present the integrated system results and the overall system efficiency. Additionally, avenues for further improving the system efficiency are discussed. Lastly, in the final chapter of the thesis, the results are summarized and the next steps for implementing the technology are presented.

## **2 Microcombustor**

### **2.1 Previous Work: Combustion Portable Power Systems with TPV**

The development of portable power TPV systems was first initiated by the U.S. Army. Army interest in the technology developed in the 1960's shortly after the approach was first conceived. Desirable attributes of a TPV-driven portable power system include lighter weight loads, silent operation, fuel-flexibility, and instantaneous "recharging" simply by refilling the fuel supply. Despite these advantages, no practical systems have moved beyond the lab [6]. Significant further research and development is required. In particular, there is a need for improvement in system efficiencies, ruggedness of system, and thermal management. Systems have been designed on a variety of scales, as discussed here.

#### **2.1.1 Macro-Scale Burners**

The majority of macro-scale TPV research has been spearheaded by Lewis M. Fraas of JX Crystals. In 1999, JX Crystals started a collaboration with Thermo Power Corporation to research propane-fueled TPV systems [7][8]. They set out to build a 25-watt propane-fueled TPV power source to be used in combination with a rechargeable battery, Figure 2-1. The TPV burner-emitter consisted of a coaxial radiant tube configuration made of silicon carbide and incorporated tungsten and platinum emitters. A gallium antimonide (GaSb) TPV cell was used with the emitter heated to around 1400°C. The overall system, however, was only 3% efficient. It was posited that the system could reach 7% with additional filtering and heat loss reduction.

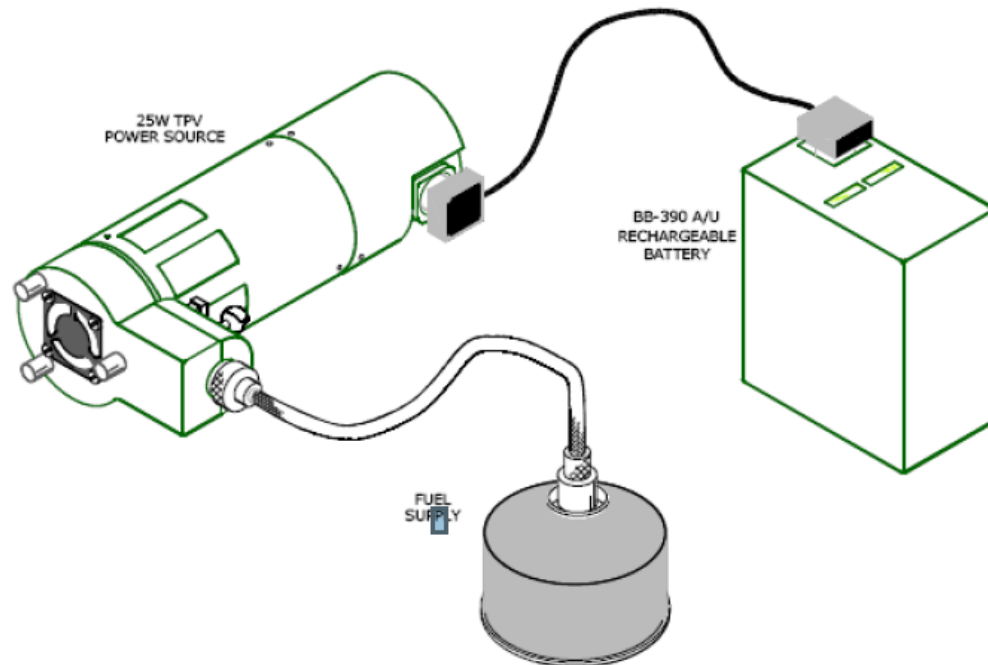


Figure 2-1: Original TPV Design [8]

More recently JX Crystals has expanded on this work, modeling a TPV battery charger with a projected fuel-to-electricity conversion of 10.9% based on computational fluid dynamic calculations (Figure 2-2) [9]. The improved design includes a new recuperator and emitter. JX Crystals developed cobalt and nickel doped ceramic matched infrared emitters for this system. The emitter would run at a temperature of 1200°C. Assuming 10% efficiency, this design would lead to 697 W-hr. of power. Advantages of this design include lighter system weight, 6.5 times higher specific energy, and an operation time 7 times that of a Li-battery. A prototype of this design, however, has not yet been made.

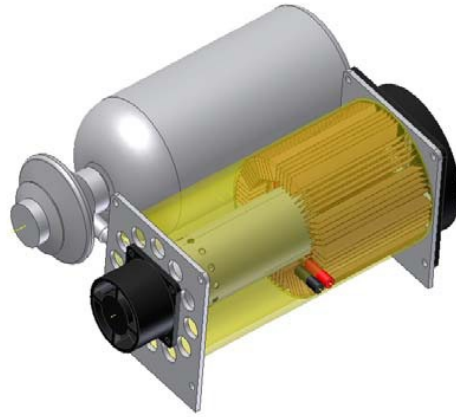


Figure 2-2: JX Crystal TPV battery with fuel cylinder 2011 Design [9]

### 2.1.2 Micro-Scale Burners

While macro-scale systems are relatively easy to fabricate, a smaller, micro-scale system is desirable as it would enable higher energy densities and allow for portable applications. As such, micro-combustion systems have been proposed. However, as the length scale of a burner decreases, the ratio of the surface-area-to-volume ( $S/V$ ) increases and maintaining a high temperature becomes increasingly difficult since heat generation scales with volume and heat loss scales with surface area.

More precisely, in order for complete combustion to occur, the residence time must be longer than the chemical reaction time [1]. An increase in surface area increases the destruction of radical species at the wall, increasing the chemical time. Simultaneously, the decrease in reactor volume reduces the residence time. The increase in chemical time and decrease in residence time lead to increased heat losses and may prevent the start of combustion or lead to quenching of an ongoing reaction.

The increase in heat loss for micro-scale systems must be accommodated through thermal management. Thermal isolation is required to reduce radical depletion at the walls and heat loss through the walls. Increasing reactant temperatures and using stoichiometric mixtures may help to reduce heat losses.

Additionally, a catalyst can be used to lower the activation energy of the reactants. This leads to faster mass transfer and lowers the critical operating temperature for which self-sustaining reactions can occur [10]. In this way, catalytic combustion reduces the heat losses associated with micro-scale systems and also decreases thermal stresses. Moreover, catalytic systems are easier to ignite and self-sustain the reaction at leaner fuel/air ratios.

Propane/air mixtures can be ignited at less than 200°C if a platinum catalyst is deposited on the surface. Sitzki *et al.* recorded ignition at 275°C for 2% propane and at 190°C for 3% propane with a platinum catalyst [11]. Norton and Vlachos also studied the effects of a platinum catalyst on ignition properties [12]. With externally applied resistive heating they recorded ignition at 151°C when 30 W of power was supplied (at an equivalence ratio of  $\Phi = 0.77$ ). At this point, the system ignited and the temperature jumped to 676°C (Figure 2-3, note that temperatures are recorded in Kelvin).

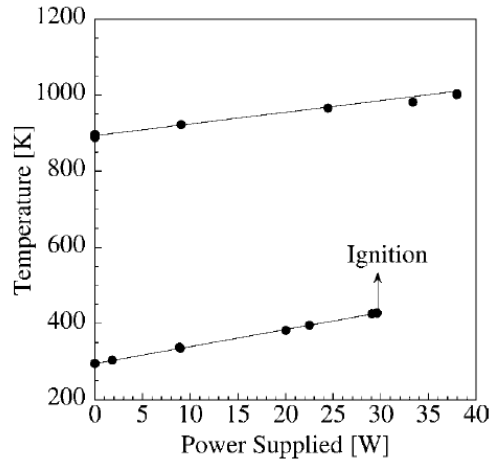


Figure 2-3: Temperature vs. power supplied [12]

Initially, it was believed that there was a critical dimension ( $\sim 1\text{mm}$ ) below which flame propagation could not be achieved due to the thermal and radical quenching as described previously [13], [14]. However, work within the past ten years has shown that it is possible to sustain a flame in certain ceramic microstructures [15–18]. These micro-TPV systems, however, have only produced power in the range of milliwatts, with only one research group achieving 1 W [19].

## **2.2 Our Approach**

Although the energy density of a combustion system increases with decreasing size, the power output of TPV cells decreases with decreasing surface area. As such, a meso-scale system is the most appropriate choice for a portable TPV-powered combustion system. A meso-scale system benefits from decreased size and weight as compared to a macro-scale system and increased power with increased TPV cell area as compared to micro-scale systems. Moreover, a meso-scale TPV-CFR system may eliminate the issues of flame quenching associated with micro-scale systems. Despite these advantages, meso-scale systems have yet to be developed. This thesis seeks to design a meso-scale TPV-CFR system to develop power in the range of 1-50 watts.

## **2.3 Design Details**

### **2.3.1 Catalytic Flow Reactor**

The body of the catalytic flow reactor is a modular, three-plate chamber. The chamber is made from alumina which has a high operating temperature, melting point of 2,072°C, low coefficient of thermal expansion, and is relatively easy to fabricate. Alumina also has a relatively high thermal conductivity (30 W/m·K), which allows for greater heat transfer through the chamber wall to the emitter.

The chamber has six inlets for even dispersion of the fuel/air mixture across the catalyst. There are also six exhaust outlets. In order to create a secure seal, a high temperature Fiberfrax paper was used as a gasket material in between the plates.

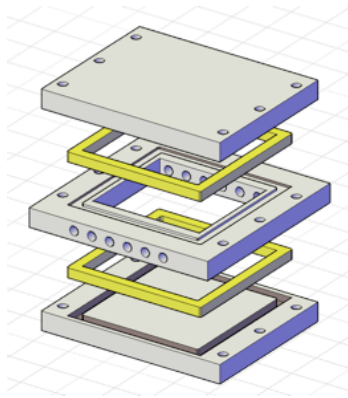


Figure 2-4: Combustion chamber and gasket: The chamber consists of three plates which

A platinum-plated nickel catalyst is employed inside the chamber. Platinum and nickel were chosen since they are known to be good catalysts; platinum and nickel both adsorb well enough to hold and activate reactants, but not so strongly that the products do not desorb. Moreover, it has been shown that platinum catalysts can extend both lean and rich extinction limits[20]. The procedure for producing the catalyst is detailed in the Appendix A.

The emitter is made of silicon carbide, SiC, which has desirable attributes: high thermal conductivity (50-120 W/m·K), stability at high temperatures, a high melting point of 2,380°C, and high emissivity at desirable wavelengths (Figure 2-5). The SiC emitter sits on top of the chamber. The heated emitter radiates upward toward three cell holder plates which hold up to three TPV cells each. The cooling chamber rests on top of the cells and is coated with an electrically insulating, thermally conductive paste.

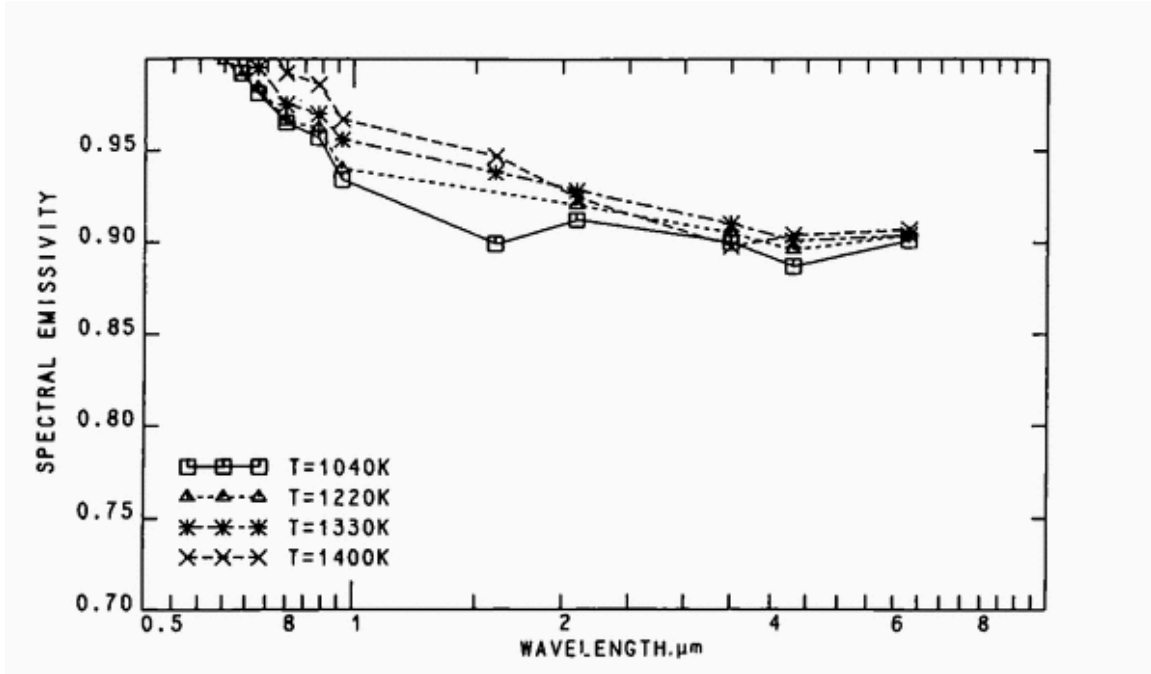


Figure 2-5: The spectral emissivity of SiC at varying high temperatures. SiC has a high emissivity at the desirable wavelengths (<1.74μm). [21]

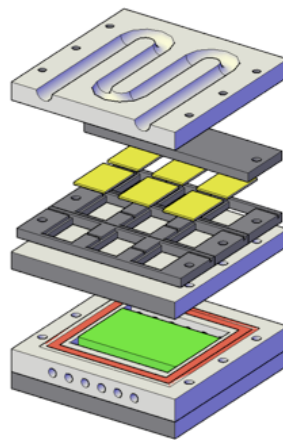


Figure 2-6: Exploded view of chamber: The catalyst (green) sits inside the chamber. Three cell holder plates can hold up to nine TPV cells (yellow). A cooling chamber keeps the TPV cells at low temperatures.

The fuel and air lines are fed through Matheson flow meters and flashback arrestors. They mix upstream of the combustor, enter a manifold, and are dispersed into six channels that feed into the chamber. There, the reactants diffuse toward the catalyst; if the catalyst is above the critical ignition temperature and the mixture is within the flammable limits, ignition occurs and heat is transferred through the chamber walls to the emitter. The temperature of the catalyst and the chamber air are measured by type K thermocouples and a Stanford Research Systems thermocouple monitor.

### **2.3.2 Fuel Choice**

Out of all of the simple alkanes, propane ( $C_3H_8$ ) is the most suitable for our system. Propane has a higher energy density per unit volume and lower activation energy for combustion than methane ( $CH_4$ ). Propane also has a higher vapor pressure than other fuels, such as butane ( $C_4H_{10}$ ), and therefore results in less condensation.

Various propane-fueled combustion experiments have incorporated hydrogen for pre-heating the chamber. However, the high strength tanks required to store compressed hydrogen drastically lower the system energy density, negating the desired benefits of the high energy density of the fuel. As such, hydrogen gas is not employed in our system.

## **2.4 Experiment and Results**

### **2.4.1 Power Goal and Flow Rates**

The energy density,  $u$ , of propane is 46kJ/g. To generate 50W, assuming a 5% overall system efficiency, we aim to generate 1kW. For 1kW the required mass flow of

the propane/air mixture is then 22 mg/s, as determined by Equation 2.1. Since the mixture is a 6:1 excess air molar ratio, 22 mg/s corresponds to 17.5 mg/s (892 sccm) of air and 4.5 mg/s (151 sccm) of propane. The flow rate calculations are detailed in Appendix B.

$$Q_{comb} = u * f \quad 2.1$$

#### **2.4.2 Adiabatic Flame Temperature**

The adiabatic flame temperature,  $T_{ad}$ , is the maximum combustion temperature possible – the temperature that the combustion products will obtain if no energy is lost to the outside environment. The adiabatic flame temperature is calculated using Cantera [22], an object-oriented toolkit for chemical kinetics and thermodynamics. The adiabatic flame temperature for a fuel-air equivalence ratio of 0.83 using propane fuel is 1814°C.

#### **2.4.3 Ignition**

##### **2.4.3.1 Flammable Range**

Gas mixtures will only burn if the fuel concentration lies within certain limits. The fuel concentration range that is burnable upon ignition is the explosive or flammable range. The lower bound is the lower flammable limit (LFL); below the LFL the mixture will be too fuel-lean to burn. The upper bound is the upper flammable limit (UFL); above the UFL, the mixture is too fuel-rich to burn. For propane, the flammable range occurs for propane concentrations between 2.1-10.1% by volume in air. For a stoichiometric 5:1 molar ratio of air to fuel, propane is 4.2% by volume. For the fuel lean mixture with a

6:1 ratio, the concentration is 3.5% by volume and our mixture is, therefore, within the flammable range, albeit closer to the LFL.

#### **2.4.3.2 Preheating:**

To ignite propane/air mixtures, external heating is necessary. The auto-ignition temperature of propane in air is between 493°C and 548°C. When employing a catalyst, however, ignition temperatures are much lower. The catalyst must reach a critical threshold temperature  $T_c$  to ignite the heterogeneous surface reaction. Ignition is indicated by a sudden jump in temperature. As power going to the catalyst is decreased, the reaction is extinguished at a lower temperature than  $T_c$  [23].

Ignition temperatures for catalysts in micro-scale burners (characteristic length less than 1mm) are well documented and were described in Section 2.1.2. It has been shown that the ignition characteristics of small-scale devices are qualitatively different, however, than their conventional-sized counterparts, mostly due to heat losses when the device is warming up [24][25]. The auto-ignition temperature in a meso-scale system is expected to differ with ignition characteristics somewhere between that of micro- and macro-scale combustors.

#### **2.4.4 Combustion Efficiency**

The overall combustion efficiency is the product of the chemical efficiency and the thermal efficiency. The chemical efficiency, Equation 2.2, is the ratio of total heat generated to the total energy that is contained within the fuel, where,  $\dot{m}_a$  and  $\dot{m}_f$  are the air and fuel mass flow rates [g/s] and  $h$  is the specific enthalpy [J/g]. The heat flow lost

to the surroundings is given by ( $\dot{Q}_{loss}$ ) [J/s]. The thermal efficiency, Equation 2.3, is the ratio of the heat gained by the gas to the total heat generated. The overall efficiency is the product of the chemical and thermal efficiencies and is given by Equation 2.4; it is the ratio of the heat retained by the gas to the energy content of the fuel.

$$\eta_{chemical} = \frac{[(\dot{m}_a + \dot{m}_f)h_{exit} - \dot{m}_a h_{inlet}] + \dot{Q}_{loss}}{\dot{m}_f h_f} \quad 2.2$$

$$\eta_{thermal} = \frac{(\dot{m}_a + \dot{m}_f)h_{exit} - \dot{m}_a h_{inlet}}{[(\dot{m}_a + \dot{m}_f)h_{exit} - \dot{m}_a h_{inlet}] + \dot{Q}_{loss}} \quad 2.3$$

$$\eta_{combustion} = \frac{(\dot{m}_a + \dot{m}_f)h_{exit} - \dot{m}_a h_{inlet}}{\dot{m}_f h_f} \quad 2.4$$

The specific enthalpy is the product of the specific heat ( $c$ ) [kJ/kg\*K] and the temperature ( $T$ ), where specific heat is the amount of heat required to raise the temperature by one degree Celsius. Making this substitution, Equation 2.4 becomes Equation 2.5. Using the known specific heat values, flow rates, and measured temperature, we can calculate the efficiency of the combustion system.

$$\eta_{combustion} = \frac{(\dot{m}_a + \dot{m}_f)cT_{exit} - \dot{m}_a cT_{inlet}}{\dot{m}_f h_f}$$

2.5

### 2.4.5 Results

The chamber atmosphere was preheated to 300°C. An excess-air molar ratio of 6:1 was employed, as discussed in Section 2.4.1. Combustion was achieved as indicated by a 263°C jump in temperature over the course of five seconds, Figure 2-7. The combustion temperature peaked at 550°C which is much lower than the adiabatic flame temperature. Using Equation 2.5, this yields a combustion efficiency of only 7.4%. The same catalyst sample was re-tested but combustion was not achieved.

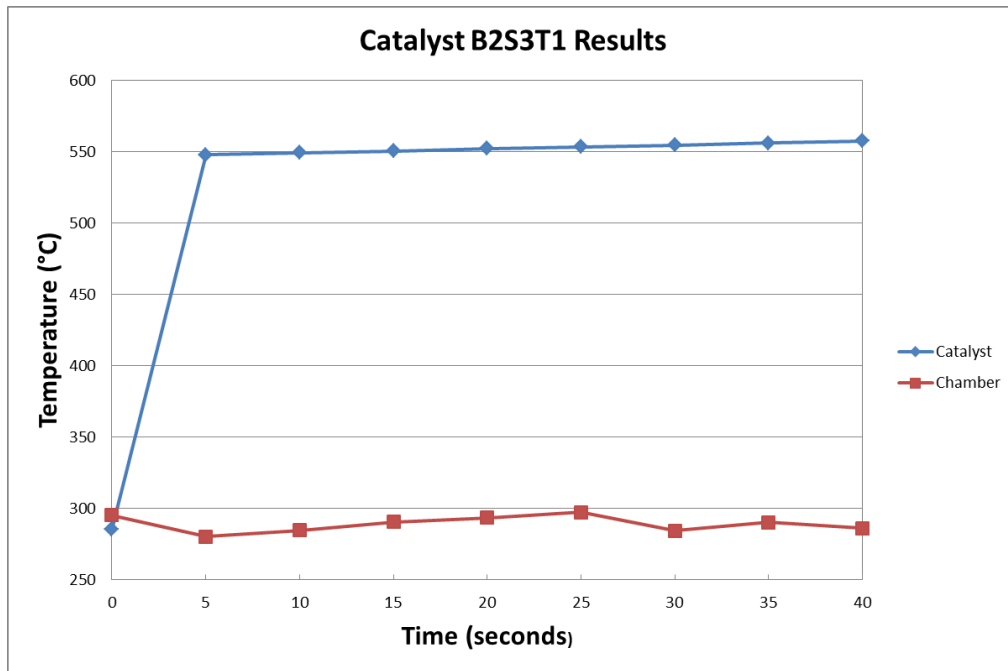


Figure 2-7: Combustion results: combustion was indicated by a 263°C jump in temperature of the catalyst over the course of five seconds.

The catalyst was examined and markings on the catalyst indicated that combustion had only occurred on one side, as can be seen in Figure 2-8. This is probably due to a block in the thin tubing leading into the CFR. Moreover, since the catalyst was unable to reproduce combustion results, it was hypothesized that the surface had been contaminated.

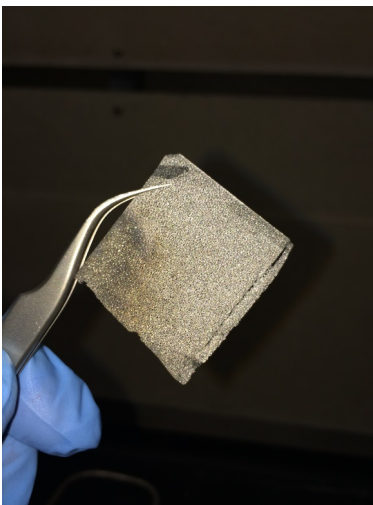
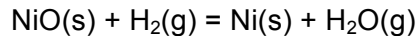


Figure 2-8: Catalyst post-combustion testing: blackened marks indicate combustion only occurred on one side of catalyst.

X-Ray Photoelectron Spectroscopy (XPS) measurements were performed with a Thermo Scientific K-Alpha system to determine the elemental composition of the surface of the catalysts. XPS spectra revealed that post-testing, catalyst samples had no platinum on the surface and instead were covered by a nickel oxide layer. A surface treatment was developed to remove the nickel oxide from the surface. This treatment included first heating the samples to 700°C to remove any carbon contamination and subsequently flowing hydrogen gas over the samples to reduce the surface and uncover the platinum. The reduction stoichiometry is as follows:



XPS characterization revealed that treated samples had an improved platinum content of ~30%. These samples were etched to reveal the chemical composition beneath the surface. Platinum content of 67% was revealed after the first etch and up to 72% after the second etch. An XPS spectrum of the catalyst surface post-etching is shown in Figure 2-9. The peak at 100eV indicates the high platinum content just below the surface.

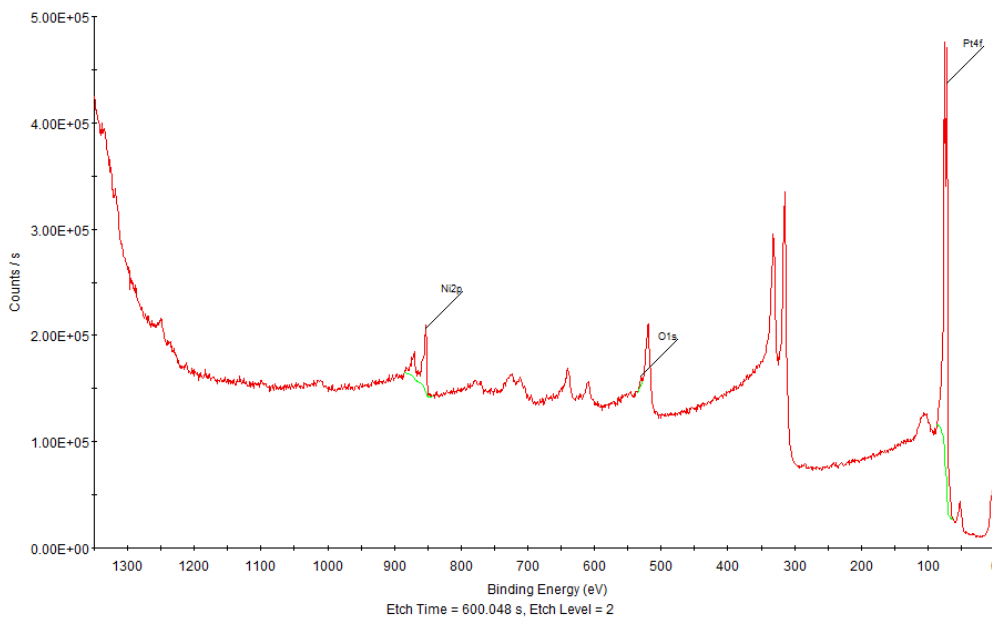


Figure 2-9: XPS spectrum of the etched catalyst surface. The sharp peak at ~100eV indicates a high concentration of platinum.

Samples with surface treatment underwent testing but did not result in combustion. Post-testing, this sample was characterized by XPS and revealed no surface platinum content; however, etching of the catalyst surface revealed platinum beneath the surface, as in the case of the treated non-tested control sample. The

elemental compositions of the tested and non-tested treated catalyst samples are listed in Table 2-1. Note that compositional values of 7% or less are not accurate due to the sensitivity of the XPS system.

Pre-etch	Control	Tested
Pt	31.35	~0
O	47.45	57.11
Ni	21.20	40.80
<b>After 1<sup>st</sup> Etch</b>		
Pt	67.41	67.79
O	<7	12.42
Ni	32.59	19.79
<b>After 2<sup>nd</sup> Etch</b>		
Pt	72.43	70.70
O	<7	8.66
Ni	27.57	20.64

Table 2-1: Elemental composition of surface treated samples before and after testing

While the treatment was successful at recovering some of the platinum, the maximum platinum content contained in the bulk of the catalyst was not obtained. Moreover, as stated, tests with treated surfaces that had ~30% platinum content did not yield combustion across any ratio of flue gases. As such, further experiment adaptations, such as improved thermal insulation, must be put in place in order to produce reliable results.

## 2.5 Chapter Summary

In this chapter we presented the motivation, design, and implementation of a catalytic combustion system for powering TPV devices. Scale of the system is an important factor in optimizing the operation of the TPV-CFR. While micro-scale combustion systems boast higher energy densities, radical depletion at the vessel walls lead to quenching of the reaction, as discussed in Section 2.1.2. For larger vessels, the ratio of the surface area to the volume decreases, decreasing the likelihood of free radical absorption and lowering the auto-ignition temperature. In fact, auto-ignition temperature is inversely proportional to the logarithm of the vessel size. Additionally, the increased overall surface area allows for the incorporation of more TPV diodes and a larger power output. A meso-scale combustor has the advantages of a larger system while remaining small enough to be portable. As such, we designed and produced a meso-scale catalytic flow reactor for powering TPV devices.

Our TPV-MFR system was fueled by a fuel-lean mixture with a 6:1 ratio of air to propane. The system incorporated a platinum-plated nickel catalyst to lower the activation energy and, therefore, the auto-ignition temperature. The system was heated externally and ignition occurred when the catalyst reached a temperature of 285.7°C, as opposed to the regular auto-ignition temperature of 540°C. Combustion was indicated by a 263°C jump in temperature over the course of five seconds, with the reaction peaking at 550°C. This relatively low temperature resulted in a combustion efficiency of only 7.4%. Moreover, catalytic combustion results were not repeatable in a consistent manner. Analysis of the catalyst surface by XPS revealed that post-combustion the catalyst was covered in a thick nickel oxide layer. It was hypothesized that removing this oxide layer would improve the combustion reaction. A surface treatment was developed to remove the oxide layer through heating and subsequently reducing the surface in a

hydrogen environment for at least 8 hours. The catalyst surface was examined post-treatment to reveal that the oxide was removed. However, the treated surface only contained 30% platinum content, while the bulk material has a content of ~70%, as proven by etching through the surface with the XPS system. Moreover, further experiment adaptations, including improved thermal insulation, must be included to improve the catalytic reaction.

## **3 Thermophotovoltaics**

### **3.1 Introduction**

This chapter details the design and development of long wavelength thermophotovoltaic (TPV) diodes. First detailed background is provided on basic photovoltaic diode physics. Motivation for longer wavelength diodes is presented and challenges associated with longer wavelength diodes are discussed. In order to circumvent the issues associated with long wavelength diodes, we propose here a monovalent barrier superlattice design. The structure design and simulation results of the barrier superlattice diodes are then presented.

### **3.2 Photovoltaic Background**

The energy converter of a thermophotovoltaic system is a photodiode – a two-terminal semiconductor that converts light into electricity. In order to understand how a TPV diode works, we must first understand the semiconductor physics of the diode.

#### **3.2.1 Conductors, Semiconductors, and Insulators**

Power is produced through the generation of a current and a voltage. A current consists of a uni-directional stream of flowing charge. In order to have mobile charges, the charge must first be freed from the atoms they are bound to, and then subsequently pulled in one direction. The outermost electrons bonded to the atom are said to be in the valence band. If this bond is broken and the electron is freed, the electron is said to be in the conduction band. The difference in energy between the conduction band and valence band energies is the bandgap energy, denoted  $E_G$ . The energy levels can be

represented on a band diagram as shown in Figure 3-1. Additionally, the energy level at which a state has a 50% change of being occupied is the Fermi level.

The amount of energy required to break the bond of the electron from the atoms varies greatly depending on the type of material. If the bandgap is large,  $>3\text{eV}$ , the material is an insulator. If the conduction band and valence band overlap, the material is a conductor. For small bandgaps, the material is a semiconductor. Semiconductor materials are the crux of photovoltaic devices.

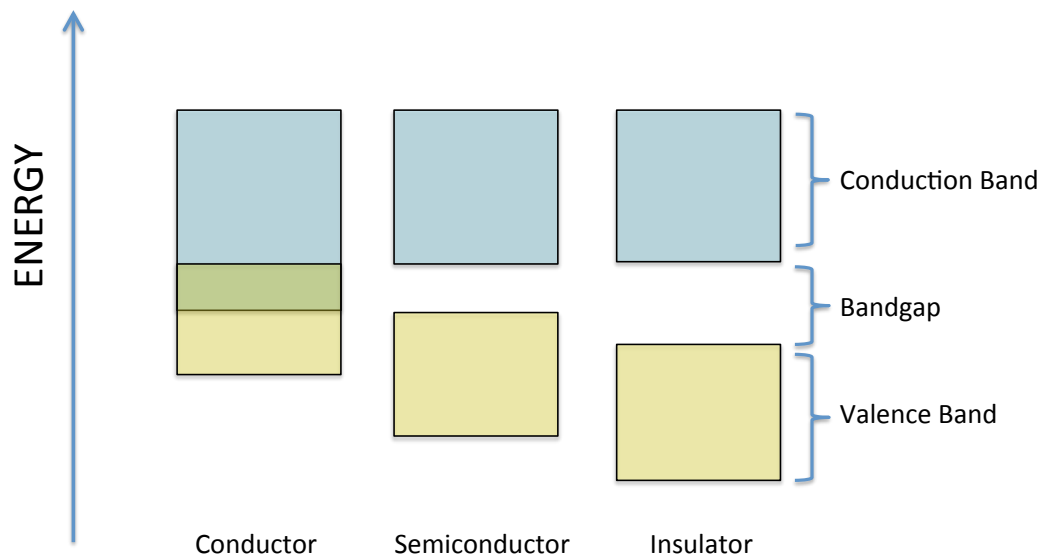


Figure 3-1: Band diagram representation for conductors, semiconductors, and insulators.

Generation of current through the photovoltaic mechanism is a two-step process. In the first step, the energy from the absorption of a photon is transferred to the excitation of an electron from an atom, freeing the electron to the conduction band and leaving a “hole” or lack of electron in the valence band. In the second step, charge carriers must be swept uni-directionally together to produce a current. This is achieved by establishing an electric field within the material. An electric field can be set up within

a material through having a net positive charge on one side of the device and a net negative charge on the other side of the device. In semiconductor materials, this is achieved internally through “doping” of the material, in which impurity atoms are added in such a way as to create a net positive or negative charge, as described in the following section.

### 3.2.2 Doping

A material is considered intrinsic if the Fermi level is mid-gap. The effective conduction and valence density of states ( $N_c$  and  $N_v$ ) are given by Equations **3.1** and **3.2**, where  $m_e$  and  $m_h$  are the effective electron and hole masses,  $k_B$  is Boltzmann’s constant,  $T$  is the temperature, and  $\hbar$  is the reduced Plank constant. The conduction and valence band densities are dependent on the effective electron and hole masses,  $m_e^*$  and  $m_h^*$ , which are the masses of the carriers adapted to include the forces experienced by the carrier within the crystal lattice. The intrinsic number of carriers in a material at any given point is dependent on the effective density of states, the bandgap, and the temperature and given by Equation **3.3**. A material can be made extrinsic through the process of doping, in which impurity atoms are added to the material to introduce extra electrons or holes.

$$N_c = 2 \left( \frac{m_e^* k_B T}{2\pi \hbar^2} \right)^{3/2} \quad 3.1$$

$$N_v = 2 \left( \frac{m_h^* k_B T}{2\pi \hbar^2} \right)^{3/2} \quad 3.2$$

$$n_i = \sqrt{N_c N_v} e^{-\frac{E_g}{2kT}}$$

3.3

For example, a negatively doped or “n-type” material is created by adding a large amount of donor atoms that contain extra electrons. These donor atoms create extra energy states near the conduction band edge. Since the energy difference between these introduced impurity levels and the conduction band edge is small, at room temperature the electrons from these donor atoms are excited to the conduction band. Since more electrons are moved to the conduction band, this causes the Fermi level to shift up (Figure 3-2, left).

Similarly, a positively doped “p-type” material is made by doping a material with acceptor atoms, which have one less electron. The doping of acceptor atoms creates energy states near the valence band edge. At room temperature, these atoms ionize, as electrons from the valence band move to fill these holes. We can also think of this process as “holes”, or positive charge, moving into the valence band. Since more holes are in the valence band, the Fermi level shifts downward (Figure 3-2, right).

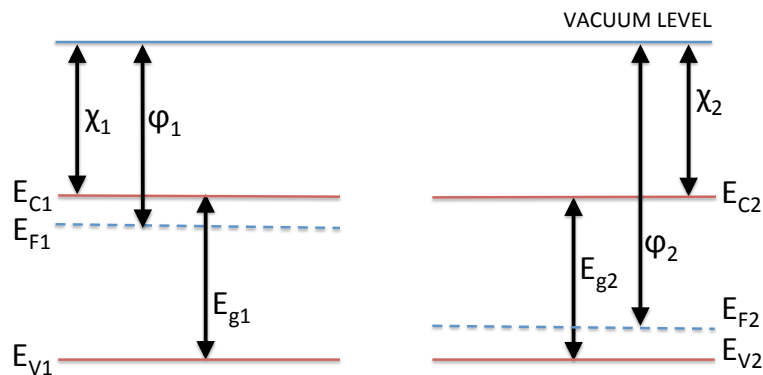


Figure 3-2: N-type (left) and p-type (right) band structures. In an n-type material, the high doping of donor atoms shifts the Fermi level upward. In a p-type material, the high doping of acceptor atoms shifts the Fermi level downward.

### 3.2.3 The PN Junction

P-type and N-type doped materials can be combined together to set up an electric field within the material. Upon interfacing a p-type and n-type material together to form a heterojunction, the excess electrons from the n-type material will diffuse into the p-type material, recombining with holes as they diffuse. Likewise, excess holes of the p-type material will diffuse into the n-type material, recombining with electrons as they diffuse. As the carriers recombine, positive ions are uncovered in the n-type region and negative ions are uncovered in the p-type region. The region of ions forms the space charge region (SCR), also called the depletion region since the charge carriers have been depleted. An electric field is set up between the positive and negative ions within the depletion region.

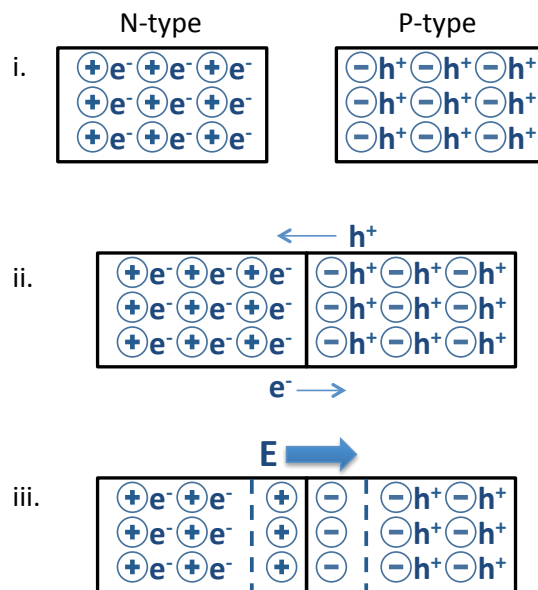


Figure 3-3: i. Isolated n-type and p-type materials ii. Electrons from the n-type material diffuse into the p-type material, recombining with holes; holes from the p-type material diffuse into the n-type material, recombining with electrons iii. Positive ions are uncovered in the n-type region; negative ions are uncovered in the p-type region. An electric field is set up between the two depleted regions.

Since the Fermi level remains constant in equilibrium under zero applied bias, the formation of a heterojunction between the n-type and p-type materials leads to band bending (Figure 3-4). The electric field stretches over the band bending region.

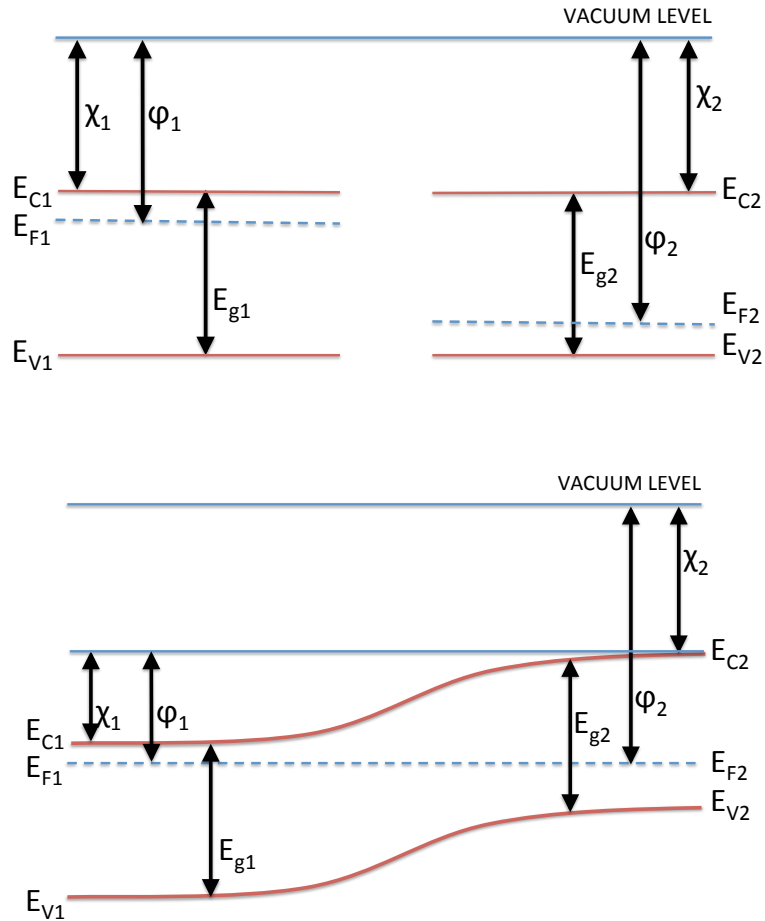


Figure 3-4: Band diagrams for isolated n-type and p-type materials (top) and the heterojunction pn diode (bottom). For the n-type material, the Fermi level is close to the conduction band edge. For the p-type material, the Fermi level is close to the valence band edge. The Fermi level remains constant for any material under zero bias; thus, when the p and n materials are combined to form a heterojunction, band bending occurs. The built-in potential and electric field occur throughout the band-bending region.

### 3.2.4 The Ideal Diode Current

The built-in potential and doping profile of the diode result in a drift and diffusion current, respectively (Figure 3-5). The diffusion current results from majority carriers with enough energy to overcome the barrier and move across the junction. The drift current arises from minority carriers, electrons in the p-region “ $n_p$ ” and holes in the n-region  $p_n$ , within a diffusion length of the SCR that diffuse to the SCR and are subsequently swept up by the electric field, creating a current, Figure 3-5. This current depends on the concentration of minority carriers multiplied by the effective velocity at which they reach the SCR, which is the ratio of the diffusivity,  $D$  to the diffusion length,  $L$ , the average distance the carriers travel before recombining (Equation 3.4). The diffusivity is proportional to the mobility and is given by Equation 3.5. The diffusion length is proportional to the square of the diffusivity and the minority carrier lifetime, Equation 3.6. Using the fact that  $np=n_i^2$ , (and therefore  $N_D p_n=n_i^2$  and  $N_A n_p=n_i^2$ ) the drift current density can be rewritten in terms of the intrinsic carrier concentration and the doping, Equation 3.7. Note that, if one side of the junction has a much higher doping concentration, that side will have a lower minority carrier concentration, and the drift current density will be dominated by the lower doped side.

$$I_0 = qA \left( \frac{D_n}{L_n} p_n + \frac{D_p}{L_p} n_p \right) \quad 3.4$$

$$D_{n,p} = \frac{kT}{q} \mu_{n,p} \quad 3.5$$

$$L_{n,p} = \sqrt{D_{n,p} \tau_{n,p}} \quad 3.6$$

$$I_0 = qAn_i^2 \left( \frac{D_n}{L_n} \frac{1}{N_D} + \frac{D_p}{L_p} \frac{1}{N_A} \right) \quad 3.7$$

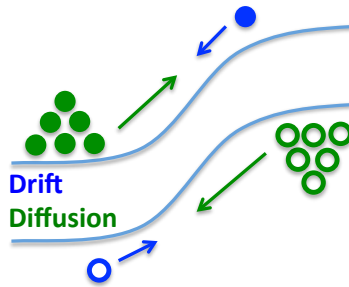


Figure 3-5: Visualization of drift and diffusion currents. Electrons are represented by solid circles and holes are represented by open circles. Minority carriers, which result in a drift current, are shown in blue. Majority carriers, which result in diffusion current, are shown in green. At zero applied bias, these two currents cancel each other exactly.

At zero applied bias, the drift current and diffusion current balance each other precisely. If a reverse bias is applied to the PN junction, the barrier height increases, blocking the flow of majority carriers. Minority carriers that diffuse to the depletion region still flow, generating a reverse bias current. Since this current is limited by the probability of a minority carrier reaching the SCR, and not the strength of the electric field, this current is essentially independent of applied voltage and saturates after a few  $kT/q$ . This current is therefore known as the diode saturation current ( $I_0$ ).

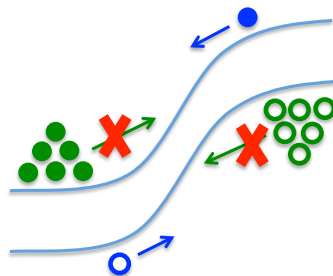


Figure 3-6: Diode currents in reverse bias. Electrons are represented by solid circles and holes are represented by open circles. Minority carriers, which result in a drift current, are shown in blue. The high barrier in reverse bias blocks majority carriers.

An applied forward bias decreases the barrier height. The same small number of minority carriers that wander into the SCR drift across the SCR, but now more majority carriers are able to overcome the barrier, injecting themselves across the SCR where they become minority carriers. As the injected carriers diffuse further into the material, they recombine with majority carriers. As such, a gradient of minority carriers results in the flatband region, generating a diffusion current. This current increases exponentially with increasing bias.

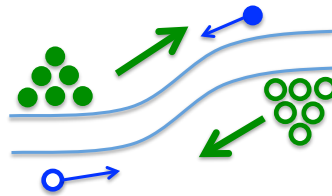


Figure 3-7: Diode current mechanism in forward bias. Electrons are represented by solid circles and holes are represented by open circles. Minority carriers, which result in a drift current, are shown in blue. The barrier height decreases with increasing applied forward bias, and the diffusion current due to the majority carrier injection increase exponentially.

Since the PN junction has only a very small current in reverse bias and a large current in forward bias, it exhibits a rectifying behavior (Equation 3.8). The current-voltage curve looks like that in Figure 3-8. Substituting in the for the saturation current, the ideal diode current is written as Equation 3.9:

$$I_{ideal} = I_0 \left( e^{\frac{qV_A}{kT}} - 1 \right) \quad 3.8$$

$$I_{ideal} = qA \left( \frac{D_n}{L_n} p_n + \frac{D_p}{L_p} n_p \right) \left( e^{\frac{qV_A}{kT}} - 1 \right) \quad 3.9$$

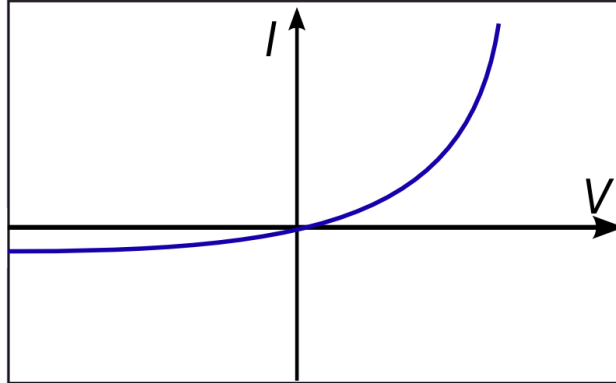


Figure 3-8: Current-Voltage curve for ideal diode. For reverse bias, the diode quickly approaches the saturation current. For forward biases, the current increases exponentially with increasing voltage.

### 3.2.5 Deviations from Ideality: The RG Current

In the previous section we described the ideal diode current, which is due to drift and diffusion of carriers from the flatband region of the diode. The ideal diode equation is accurate for diodes at low temperatures; however, at non-zero temperatures, parasitic thermal recombination-generation (R-G) processes within the depletion region generate an additional current. The total current is the sum of the ideal current (referred to henceforth as the diffusion current) and the RG current (Equation 3.10).

$$I_{total} = I_{DIFF} + I_{R-G} \quad 3.10$$

The generation-recombination current occurs due to changes in minority carrier concentrations from that of the equilibrium value in reverse/forward bias. In reverse bias, carriers are reduced at the edges of the depletion region below the equilibrium value. To compensate, hole pairs are thermally generated and swept out by the electric field, creating a *generation current* that adds to the reverse bias current. At forward biases, the minority carrier concentration is above that from the equilibrium value, resulting in recombination within the depletion region. To compensate, additional carriers are injected into the depletion region, drawn out from the contacts, creating a *recombination current*.

The rate at which recombination-generation processes occur ( $U_{GR}$ ) is the same for electrons and holes under steady-state conditions. Summing the carriers created/destroyed per second and multiplying by  $q$  gives the extra current from this process (Equation 3.11). Three types of recombination commonly occur: radiative, Auger, and Shockley-Read-Hall.

$$I_{R-G} = -qA \int_{-x_p}^{x_n} U_{GR} dx \quad 3.11$$

### **Radiative**

In radiative recombination, an electron from the conduction band directly recombines with a hole in the valence band, releasing a photon. Radiative recombination occurs primarily in direct bandgap semiconductors and can be neglected in indirect semiconductors. The radiative recombination rate is given by Equation 3.12, where  $B_{rad}$ , the radiative recombination coefficient, is a property of the material.

$$U_{rad} = B_{rad}(np - n_i^2) \quad 3.12$$

### Auger

In Auger recombination, the collision of two similar carriers causes one to be excited to a higher energy and the other carrier to recombine with a third carrier. Auger recombination is important in materials with low bandgaps and high intrinsic carrier concentrations where carrier interactions are stronger. For GaSb-based materials with bandgaps less than 0.5 eV, Auger recombination is the main non-radiative process at room temperature and limits the open-circuit voltage [26] [27]. The net Auger recombination rate is given by Equation 3.13 in which  $C_n$  and  $C_p$  are the electron and hole Auger coefficients respectively.

$$U_{Aug} = (C_n n + C_p p)(np - n_i^2) \quad 3.13$$

### Shockley-Read-Hall (SRH)

Shockley-Read-Hall (SRH) is most often the dominant mechanism of recombination and occurs due to defects in the crystal lattice which create trap states or recombination centers. SRH recombination is a two-step process. First an electron moves into a trap state; then if a hole moves to the same state, the electron and hole recombine. The SRH recombination rate is given by Equation 3.14 and is dependent on the SRH carrier lifetimes, Equations 3.15 and 3.16, in which  $v$  is the mean thermal velocity,  $\sigma$  is the capture cross section, and  $N_t$  is the trap density states.

$$U_{SRH} = \frac{(np - n_i^2)}{\tau_{n,SRH}(p + p_t) + \tau_{p,SRH}(n + n_t)} \quad 3.14$$

$$\tau_{n,SRH} = \frac{1}{v_n \sigma_n N_t} \quad 3.15$$

$$\tau_{p,SRH} = \frac{1}{v_p \sigma_p N_t} \quad 3.16$$

Integrating over this recombination rate, the RG current is given by Equation 3.17. For reverse biases greater than a few  $kT/q$ , the carrier concentrations in the depletion region become negligible ( $n \rightarrow 0$ ,  $p \rightarrow 0$ ) and the RG current reduces to that of Equation 3.18.

$$I_{RG} = qA \int_{-x_p}^{x_n} \frac{np - n_i^2}{\tau_p(n + n_t) + \tau_n(p + p_t)} dx \quad 3.17$$

$$I_{RG \text{ reverse}} = -\frac{qAn_i}{2\tau_0} W \quad 3.18$$

$$\tau_0 = \frac{1}{2} \left( \tau_p \frac{n_1}{n_i} + \tau_n \frac{p_1}{n_i} \right) \quad 3.19$$

For forward biases, the carrier concentrations cannot be neglected. The generation-recombination current varies roughly as  $\exp(qV_A/nkT)$ , where  $1 < n \leq 2$ . The parameter  $n$  is usually close to 2 and the combined forward/reverse bias RG current is given by Equation 3.20.

$$I_{R-G} = -\frac{qAn_i}{2\tau_0}W \frac{(e^{\frac{qV_A}{kT}} - 1)}{\left(1 + \frac{V_{bi} - V_A}{kT/q} \frac{\sqrt{\tau_n \tau_p}}{2\tau_0} e^{qV_A/2kT}\right)} \quad 3.20$$

### 3.2.5.1 Variation of Diode Current with Temperature

While the generation-recombination current is proportional to the intrinsic carrier concentration, the diffusion current is proportional to the square of the intrinsic carrier concentration. As such, while generation-recombination current may dominate at low temperatures, diffusion current dominates at higher temperatures, Figure 3-9. The dominant current is therefore dependent on the operation temperature of the diode.

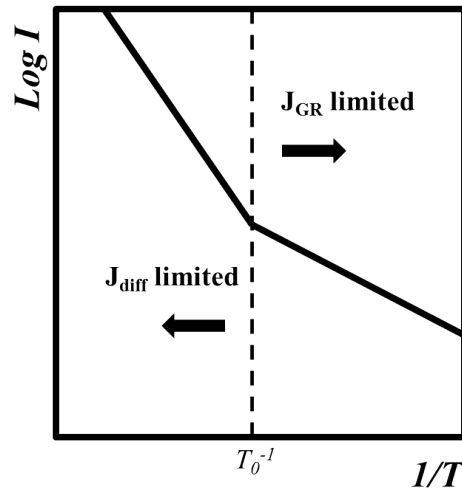


Figure 3-9: Plot of diode current versus temperature. Diffusion current is the dominant current for high temperatures and generation-recombination current is the dominant current for low temperatures. The crossover temperature is designated by  $T_0$ .

### 3.2.6 Photodiode operation

Thus far, we have described the current-voltage characteristics of a simple diode. A photovoltaic cell is a photodiode - a diode designed specifically to allow light, consisting of packets of energy called photons, to travel through the device to the SCR. If the photons have energy greater than that of the bandgap, an electron will be excited from the ground state, generating an electron hole pair (ehp). The ehp is then swept up by the electric field of the diode, generating a current in the same direction as the reverse bias current described previously. This current is referred to as the photogenerated current. For a photogeneration rate given by  $G_L$ , the current density generated due to the photo-absorption is given by Equation 3.21.

$$J_{light} = -qWG_L \quad 3.21$$

The total current is the summation of the original diode current, referred to henceforth as the dark current, with the photogenerated current. Since the photogenerated current is approximately constant for all voltages, the total current is a shifted version of the dark current curve, Figure 3-10. The power at any point on the plot is the product of the current and the voltage. The maximum power point occurs at  $(J_{MP}, V_{MP})$ . The maximum current is the short-circuit ( $J_{SC}$ ) current, which is equal to photogenerated current. The total current is given by Equation 3.22.

$$J_{total} = J_{light} + J_{Dark} = J_{SC} - J_0 \left( e^{\frac{qV}{kT}} - 1 \right) \quad 3.22$$

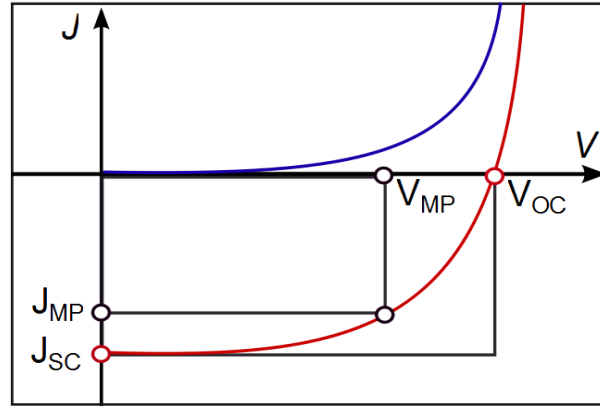


Figure 3-10: Current-voltage characteristic of an ideal diode in dark (blue curve) and light (red curve).

An important parameter is the open-circuit voltage,  $V_{OC}$ , which is the maximum obtainable voltage and occurs when the contacts are isolated and there is no current flow. The open-circuit voltage can be determined by setting the total current equal to zero in Equation 3.22; the open-circuit voltage is then given by Equation 3.23 and is proportional to the short-circuit current and inversely proportional to the dark current.

$$V_{OC} = \frac{kT}{q} \ln \left( \frac{J_{SC}}{J_0} + 1 \right) \quad 3.23$$

A common metric for characterizing the performance of a PV cell is the fill-factor - the ratio of maximum power to the product of the open-circuit voltage and the short-circuit current. Graphically, this is the ratio of the area of the small rectangle to the area of the large rectangle in Figure 3-10. The efficiency of the cell is given by the ratio of the power output to the power input and can be written by Equation 3.25.

$$FF = \frac{J_{MP} V_{MP}}{J_{SC} V_{OC}} \quad 3.24$$

$$\eta = \frac{J_{MP}V_{MP}}{P_{in}} = \frac{J_{SC}V_{OC}FF}{P_{in}} \quad 3.25$$

### 3.2.7 PV Circuit Model

A photovoltaic (PV) cell can be modeled as a current source in parallel with a diode. The total current going to the load can be approximated as the photo-generated current minus the dark current as in Equation 3.22. This equation can be modified to account for non-idealities and internal parasitic resistances (Equation 3.26). The modified equation includes the ideality factor ( $n$ ) and the series ( $R_s$ ) and shunt ( $R_{sh}$ ) resistances (as shown in Figure 3-11). The ideality factor measures how well a diode performs as compared to an ideal diode, and typically ranges from  $n=1$  to  $n=2$ . The series resistance is caused by ohmic losses through the front surface of the cell and through the metal contacts, reducing the overall voltage. The shunt resistance occurs if current is given an alternate path, reducing the overall current. Shunt resistance is due to crystal defects in the diode material. For an ideal cell, the series resistance would be zero, resulting in no further voltage drop before the load, and the shunt resistance would be infinite so that no alternate path is provided for current flow. Both series and shunt resistance can be extracted from the positive bias portion of a current-voltage curve.

$$J(V) = J_{SC} - J_0 \left( e^{\frac{q(V+IR_s)}{nkT}} - 1 \right) - \frac{V + J_0 R_s}{R_{SH}} \quad 3.26$$

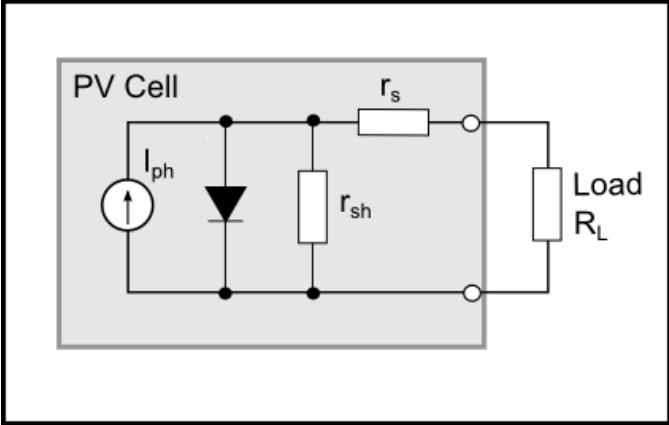


Figure 3-11: Circuit diagram for photovoltaic cell including series and shunt resistances.

### 3.3 TPV Diode Materials

Much of the progress in TPV has stemmed from developments in photovoltaics. The first implementation of TPV was in the mid-1950's when Henry Kolm of MIT Lincoln Laboratory held a silicon solar cell up to a lantern in an attempt to generate electricity from a flame [28], making silicon the first material used in TPVs. Silicon has a bandgap of 1.12 eV which corresponds to cutoff wavelength of 1.1  $\mu\text{m}$  and is therefore a good material for use with a blackbody spectrum of 6000 K, approximately the temperature of the Sun. TPV emitters, however, usually emit at 1300-2000 K, which corresponds to energies of 0.5-0.8 eV. As such, in order to employ silicon in TPV applications, silicon must be paired with selective emitters such as ytterbia,  $\text{Yb}_2\text{O}_3$ , to tailor the spectrum to the silicon diode [29], [30].

Germanium, a common bottom cell material from multi-junction solar cells, has also been used for TPV [31]. Germanium is a better match for TPV applications than silicon since germanium has a lower bandgap, 0.66eV at 300 K, and responds to wavelengths up to 1.88  $\mu\text{m}$  [30]. However, germanium is an indirect bandgap material and has a high intrinsic carrier concentration and generally poor performances. As with silicon, the conversion efficiency of a germanium TPV cell can be enhanced with the addition of a selective emitter for spectral shaping. Research has shown that an erbia radiator,  $\text{Er}_2\text{O}_3$ , radiator results in an improved spectrum for germanium cells [29], [30].

Starting in the 1980's, III-V materials consisting of two or more elements from group III and V (Figure 3-12) such as gallium antimonide (GaSb) became available [32]. GaSb-based alloys are now the leading material for TPV applications. These multi-nary compounds are most often grown epitaxially on GaSb substrates. Epitaxial growth methods include liquid phase epitaxy (LPE), liquid phase electro-epitaxy (LPEE), metal organic chemical vapor deposition (MOCVD), and molecular beam epitaxy (MBE).

Binary GaSb is in the most frequently used TPV material, 0.72 eV at 300K, and has been incorporated into commercial applications such as the Midnight Sun [33]. While initially GaSb cells were grown epitaxially, a simple Zn-diffusion process was developed to make GaSb cells out of bulk GaSb material, simplifying processing and reducing costs. GaSb has a high efficiency due to the direct bandgap nature and is cheaper than the other III-V compounds.

III		V
13 <b>Al</b> Aluminum	14 <b>Si</b> Silicon	15 <b>P</b> Phosphorus
31 <b>Ga</b> Gallium	32 <b>Ge</b> Germanium	33 <b>As</b> Arsenic
49 <b>In</b> Indium	50 <b>Sn</b> Tin	51 <b>Sb</b> Antimony

Figure 3-12: Sub-section of the periodic table showing the group III and V elements that are incorporated into TPV diode materials.

Ternary III-V materials, although more complicated and costly, allow for shorter bandgaps. InGaAs can be grown lattice matched,  $E_g=0.74$  eV, and mismatched,  $E_g=0.5-0.6$  eV, to InP substrates. InAsSb,  $E_g = 0.3$  eV, has been grown on InAs substrates with a long wavelength edge of  $4.4 \mu\text{m}$  [34]. The mixing of two different group-V elements was found to be challenging, however, due to immiscibility issues.

The addition of a fourth element for a quaternary compound makes it possible to independently vary the bandgap and lattice constant, making it easier to lattice match and removing the need for a graded buffer. However, as with the ternary compounds,

the mixing of two or more group-V elements presents epitaxial challenges. InGaAsSb can be grown to both GaSb and InAs substrates. This material has been grown with wide bandgap AlGaAsSb front surface passivating windows and back surface field cladding layers [35][36]. Although most InGaAsSb TPV diodes have been grown with bandgaps close to 0.5 eV, the InGaAsSb active layer can have a bandgap as low as 0.26 eV with high quantum efficiency out to 4.8  $\mu\text{m}$  [36]. InAsSbP has also been investigated for TPV diodes, although less so than InGaAsSb. InAsSbP is most commonly fabricated by LPE and LPEE on InAs substrates. InAsSbP has bandgaps ranging from 0.35-0.6 eV and absorption up to 3.8  $\mu\text{m}$  [37] [38].

Lastly, pentary GaInAsSbP have been grown lattice matched to GaSb by LPE. The cutoff wavelengths were in the range from 4.0-4.5  $\mu\text{m}$  at room temperature [39]. These diodes incorporate an InAsSbP window to minimize surface recombination. GaInAsSbP has the same epitaxial challenges as with other multi-nary compounds.

### **3.4 Extending the Operational Wavelength of TPV**

TPV diode bandgaps typically range in energy from 0.5–0.74eV corresponding to emitter temperatures greater than 2000°C. Shorter bandgap thermophotovoltaics are of interest because they can optimally absorb longer wavelength radiation from lower temperature sources, extending the range of applications for TPV. In fact, modeling shows advantages for narrow (<0.5eV) bandgap TPV cells [40]. In this section, we motivate and detail results for longer wavelength TPV.

### 3.4.1 Optimal Bandgap for Emitter Temperature

The radiation signature for a hot object can be approximated by a blackbody spectrum as described by Planck's Law, Equation

3.27. The peak wavelength of this spectrum is calculated through Wien's Displacement Law (Equation 3.28) where  $b = 2.897 \times 10^{-3}$  [K m].

$$B_{\lambda}(T) = \frac{2hc^2}{\lambda^5} \frac{1}{e^{hc/(\lambda k_B T)} - 1} \quad 3.27$$

$$\lambda_{max} = b/T \quad 3.28$$

One might assume that the bandgap of a photodiode should be matched to the energy value corresponding to the peak emissive power of the emitter. However, at this value, only 25% of the emissive power will have energy greater than the bandgap [41]. Since only above-bandgap photons can be absorbed, this means only 25% of the incident spectrum will be converted.

The optimal efficiency of a PV diode for an incident blackbody spectrum was originally derived by Shockley and Queisser [42]. The efficiency can be written in terms of the dimensionless bandgap parameter,  $u_g$ , which is the ratio of the cell bandgap energy,  $E_g$ , to the thermal energy,  $kT$ , of the emitter, Equation 3.29 and 3.30. Shockley and Queisser showed that the conversion efficiency is optimized for  $u_g = 2.17$ . Using this figure, for a fixed emitter temperature, the optimum bandgap can be calculated by Equation 3.31, where the emitter temperature,  $T_E$ , is in Kelvin and the bandgap is in eV [41]. Employing this equation, we observe that materials with a bandgap of 0.5 eV are only optimal for very high,  $>2000^\circ\text{C}$ , emitter temperatures, Table 3-1. To optimally

convert the incident radiation from lower temperature sources of 1,000°C, the bandgap of the TPV diode should be closer to 0.24eV, which corresponds to a cut-off wavelength around 5  $\mu\text{m}$ .

$$\eta = \frac{15}{\pi^4} u_g \int_{u_g}^{\infty} \frac{u^2}{e^u - 1} du \quad 3.29$$

$$u_g = \frac{E_G}{kT} \quad 3.30$$

$$E_{gOPTIMAL} = 1.87 \times 10^{-4} T_E \quad 3.31$$

Emitter Temperature (°C)	Bandgap for Optimal Efficiency (eV)	Cut-off wavelength ( $\mu\text{m}$ )
500	0.145	8.55
1000	0.238	5.21
2400	0.500	2.48

Table 3-1: Bandgap and cutoff wavelength for optimal conversion efficiency for various emitter temperatures.

For the ideal TPV system, perfect blackbody emitter and zero-reflectance TPV cells, the maximum power density of the system is calculated by Equation 3.32 [41]. The equation is a function of temperature of the emitter and the dimensionless bandgap energy,  $u$ , as defined by Equation 3.33. Power density is a monotonically increasing function of emitter temperature and is determined by above-bandgap photons only. A smaller bandgap increases the integration range, allowing more photons to be absorbed and converted to usable power. This can be seen in Figure 3-13 below, where the maximum power density is plotted versus temperature for several bandgap values. For an emitter temperature of 1,000°C, a cell with  $E_g=1.1\text{eV}$  allows for a power density of  $\sim 0.1 \text{ W/cm}^2$ , whereas a cell with  $E_g=0.25\text{eV}$  has a power density closer to  $10 \text{ W/cm}^2$ .

$$\frac{P_{max}}{Area} = \frac{15}{\pi^4} \sigma_{sb} T^4 u_g \int_{u_g}^{\infty} \frac{u^2}{e^u - 1} du \quad 3.32$$

$$u_g = \frac{E_G}{kT_E} \quad 3.33$$

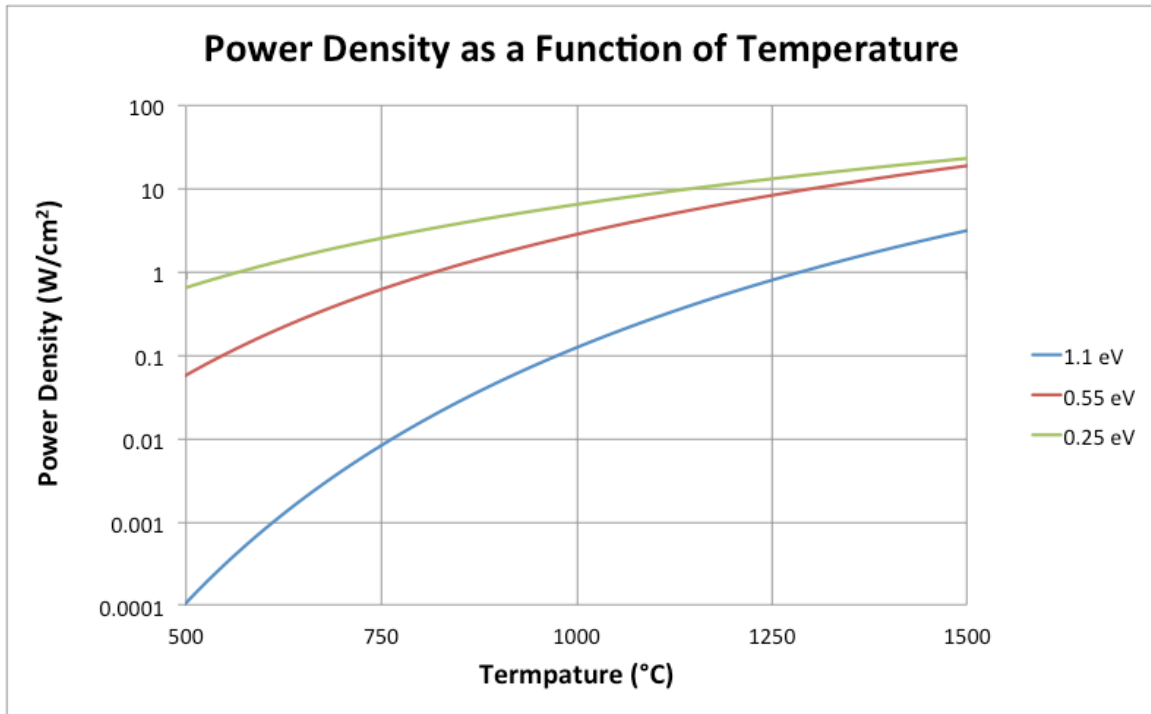


Figure 3-13: Plot of the power density of various bandgap TPV cells as a function of temperature. The shorter bandgap diodes have a higher power density. For example, the 0.25eV cell has a power density of 6.5 W/cm<sup>2</sup> at 1,000°C whereas the 1.1eV bandgap diode has a power density of only 0.06 W/cm<sup>2</sup> at 1,000°C.

As detailed in section 3.3, TPV materials have not yet been engineered to absorb beyond 5 μm. While multi-nary III-Vs can be designed to have narrow bandgaps, these materials have prohibitively large dark currents due to increased recombination processes for small bandgaps. As such, alternative material structures are required in order to circumvent these issues. In the following section we detail new approaches for

decreasing parasitic dark current in small bandgap TPV diodes, including using a superlattice and barode structures.

### **3.4.2 Decreasing recombination/reducing dark current for TPV**

#### **3.4.2.1 Superlattice Structure**

A superlattice is a structure composed of alternating, periodic thin layers of material. The idea of the superlattice was proposed by Tsu and Esaki in the late 1960s [43] and first fabricated in the 1970s. If the constituent layers of the superlattice are thin enough, on the order of nanometers, new quasi-band structures or mini-bands will form. Depending on the relative alignment of the conduction and valence bands of the two materials, the superlattice is classified as type-I or type-II. Let the superlattice be made of alternating materials A and B. In a type-I superlattice, T1SL, material A has a lower conduction band and a higher valence band than material B, creating a series of wells that confine electron and holes within material A, Figure 3-14. In a type-II superlattice, T2SL, both the conduction band and valence band of material A are lower than that of material B – confining electrons and holes to separate materials. T2SL are further classified based on the relative alignment of the conduction band of material A to the valence band of material B. If the conduction band of material A is higher than the valence band of material B, then the material is type-IIA, Figure 3-14. If the conduction band of material A is lower than the valence band of material B, then the material is type-IIB or “broken-gap,” Figure 3-14. The broken-gap structure uniquely allows for an effective bandgap that is smaller than the bandgap of either constituent layer.

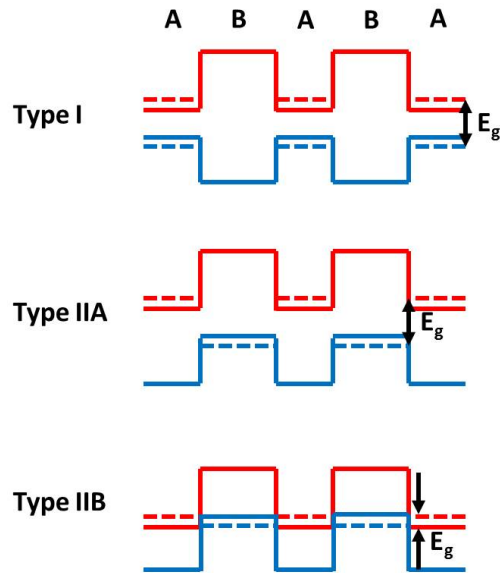


Figure 3-14: The conduction band (red) and valence band (blue) are represented by solid lines and electron and hole minibands are represented by dashed lines. There are three possible band alignments. T1SL has material A with lower conduction band and higher valence band than material B. For T2SL, both the conduction band and valence band of A are lower than that of B – confining electrons and holes to separate materials. T2SL is further classified based on the relative alignment of the conduction band of material A and the valence band of material B. If the conduction band of A is higher than the valence band of B, then the material is type-IIA. If the conduction band of A is lower than the valence band of B, then the material is classified as type-IIB.

Incorporating a superlattice for long wavelength TPV diodes has several advantages, including bandgap flexibility, reduced tunneling current, and suppressed Auger recombination. These advantages are described in more detail here.

*Bandgap flexibility:*

As stated in the previous section, the bandgap of a type-II broken-gap superlattice can be smaller than the bandgap of either of the constituent layers. An

example of type-II broken-gap superlattice is the InAs/GaSb material system, shown in Figure 3-15. The spatial band alignment for InAs/GaSb T2SL is shown in Figure 3-16; the figure shows that the conduction band of the InAs layer is lower than the valence band of the GaSb layer. Electrons are confined to InAs layers in the conduction band and the overlap of the electron wave functions between adjacent InAs layers results in electron mini-bands in the conduction band. Likewise, holes are confined to GaSb layers in the valence bands, and the overlap of hole wave functions between adjacent GaSb layers result in hole mini-bands in the valence band. The transition between these two mini-bands creates a new effective bandgap. InAs/GaSb superlattices with bandgaps ranging from 0.41 to 0.04 eV have been demonstrated [44].

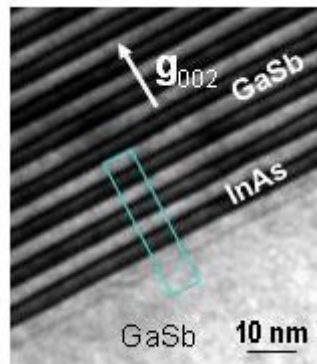


Figure 3-15: Dark-field image of a 50 period InAs/GaSb superlattice [45]

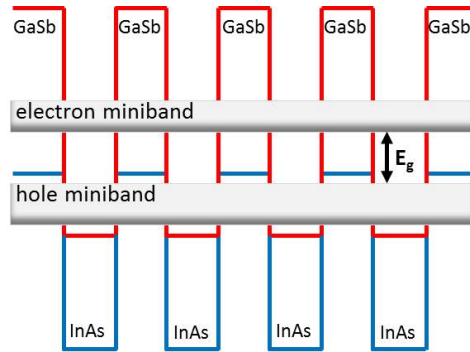


Figure 3-16: T2SL InAs/GaSb band alignment: The conduction band is shown in red and the valence band is shown in blue. The effective bandgap is the difference in energy of the electron and hole minibands, created from the overlapping wave functions of the constituent materials.

#### *Improved Effective Mass:*

In bulk materials, the carrier effective mass is determined by the interaction between the conduction band and the valence band and is therefore coupled to the bandgap. More precisely, the effective mass is inversely proportional to the bandgap by Equation 3.34 in which  $E_p$  is the Kane parameter,  $E_g$  is the energy gap, and  $\Delta$  is the spin-orbit interaction energy. Bulk semiconductors with narrow bandgaps will have carriers with small effective masses resulting in increased parasitic tunneling currents. For T2SL, on the other hand, the effective mass is mainly determined by the overlap between the electron or hole wave functions. As such, the effective mass of carriers for a T2SL does not vary with the bandgap. The T2SL, therefore, can have a larger effective mass for smaller bandgaps as compared to bulk materials leading to decreased tunneling currents.

$$m^*_{bulk} = \left[ \frac{1}{m_e} + \frac{E_p(E_g + 2/3\Delta)}{E_g(E_g + \Delta)} \right]^{-1} \quad 3.34$$

*Reduced Auger Recombination:*

In addition to improved carrier effective mass, the T2SL structure has the advantage of suppressed Auger recombination. This is because strain in the T2SL structure induces a large splitting between heavy-hole and light-hole valence sub-bands. Infrared photodetector research shows that separation of these hole bands suppresses Auger recombination, enhancing carrier lifetimes [46] [47].

The improved material properties of the T2SL structures, including bandgap flexibility and reduced parasitic currents, make it a structure of interest for lasers and other diode technologies [47] [48] [49]. T2SL have not yet, however, been developed for TPV applications. In this work we will incorporate T2SL materials into our TPV diode.

**3.4.2.2 Incorporating a Barrier**

Another avenue for improving the performance of narrow bandgap diodes is employing a barrier diode, or “bariode” structure, in which a wide-bandgap barrier is inserted into the p-n junction as in Figure 3-17. IR photodetector research has shown that the bariode structure suppresses SRH recombination for low temperature operation [50] [51]. We hypothesize that the barrier will also decrease diffusion current for room temperature operation as the barrier will block carriers that make up this current.

For our TPV cell, we study a monovalent barrier that blocks minority and majority carrier holes, Figure 3-17. Blocking the minority carrier holes reduces the diffusion

current, Equation 3.4, to that of Equation 3.35. The barrier also blocks majority carrier holes that diffuse from the p-side to the n-side in forward bias. Normally, these majority carriers face the built-in barrier that is decreased for increasing forward biases. Since this barrier is effectually increased by the introduced artificial barrier, this will lead to a delayed turn-on voltage, improving the open-circuit voltage and fill factor.

$$I_{diffusion} = qA \left( \frac{D_p}{L_p} n_p \right) \left( e^{\frac{qV_A}{kT}} - 1 \right) \quad 3.35$$

Decreasing the minority carrier concentration decreases the reverse bias saturation current. Graphically (Figure 3-18) we see that a decrease in the reverse bias enables a larger turn-on voltage for the diode. The delayed turn-on voltage will improve the open-circuit voltage and fill factor for the diode in photo-operation. Finally we note that, as photogenerated minority carriers from the p-type absorber region are not blocked by the barrier, the photogeneration current will not be compromised.

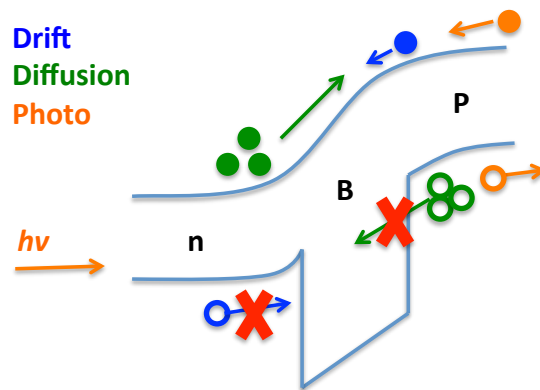


Figure 3-17: Barriere band diagram. For a monovalent barrier, minority carrier and majority carrier holes are blocked, which contribute to the dark current. Photogenerated carriers are not blocked.

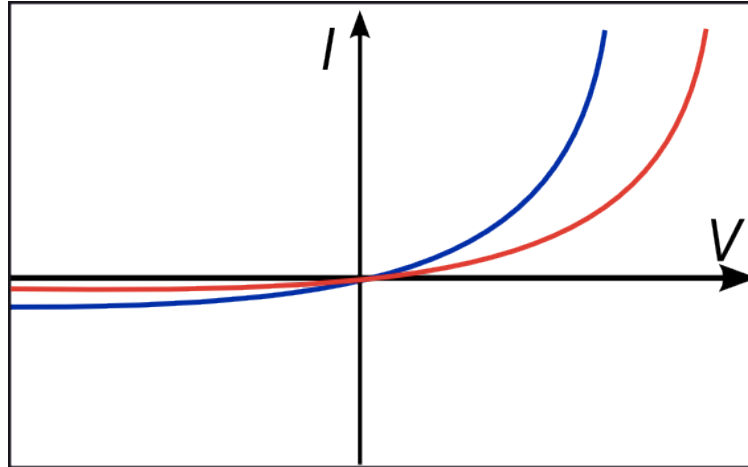


Figure 3-18: Plot comparing dark current values for two diodes. The diode with the lower saturation current is shown in red. The decreased saturation current leads to a higher turn on voltage.

Engineering the barrier structure is facilitated by incorporating superlattice materials, which, as discussed previously, enable flexibility for bandgap engineering. In the following section we present our structure and simulation results for InAs/GaSb T2SL barrier diodes.

### 3.4.3 Simulations

#### 3.4.3.1 Band Structure Design

We aim to design a diode with a smooth conduction band throughout the structure such that the barrier is entirely within the valence band. We employ an n-B-p structure, where the radiation is first incident on the n-region. The n-region must therefore be thin in order to minimize absorption and allow for transmittance of desirable wavelengths to the p-type absorber. Moreover, only photogenerated carriers within a diffusion length of the electric field will contribute to the current. As such, the electric field should extend as far in to the p-type absorber as possible.

The first design set point is the p-type absorber bandgap: this is fixed for the target cutoff wavelength. The second design constraint is the bandgap of the barrier region. The bandgap of the barrier region must be large enough such that it can have at least 100meV over the n-region and p-region bandgaps, thus creating the desired barrier.

### **3.4.3.2 Barrier and P-region**

While there are several methods for modeling the electronic bandstructure of a given material, here we employ the superlattice empirical pseudopotential method (SEPM) to model the InAs/GaSb material system [52], [53] [54]. We use the SEPM model to determine the bandstructures and bandgaps for a range of superlattices with varying ratios of InAs and GaSb monolayers. We can then generate a plot of the number of monolayers of InAs versus number of monolayers of GaSb, containing isolines of constant bandgap and constant conduction band level (Figure 3-19). We use this plot to choose the number of monolayers of InAs and GaSb to achieve the desired bandgap for the p-type absorber and barrier layer while maintaining a smooth conduction band. For our p-type absorber, we require a bandgap of 0.24eV. In Figure 3-19, the intersection of the 0.24eV bandgap contour with a constant conduction band (10 ML InAs, 13 ML GaSb) is marked. The conduction band contour can be traced down to the intersection with the 0.35eV bandgap contour (5 ML InAs, 4 ML GaSb). Since these two points have the same conduction band edge, the change in bandgap will occur entirely over the valence band. This ensures that no photo-generated electron carriers are blocked at the barrier/absorber conduction band interface.

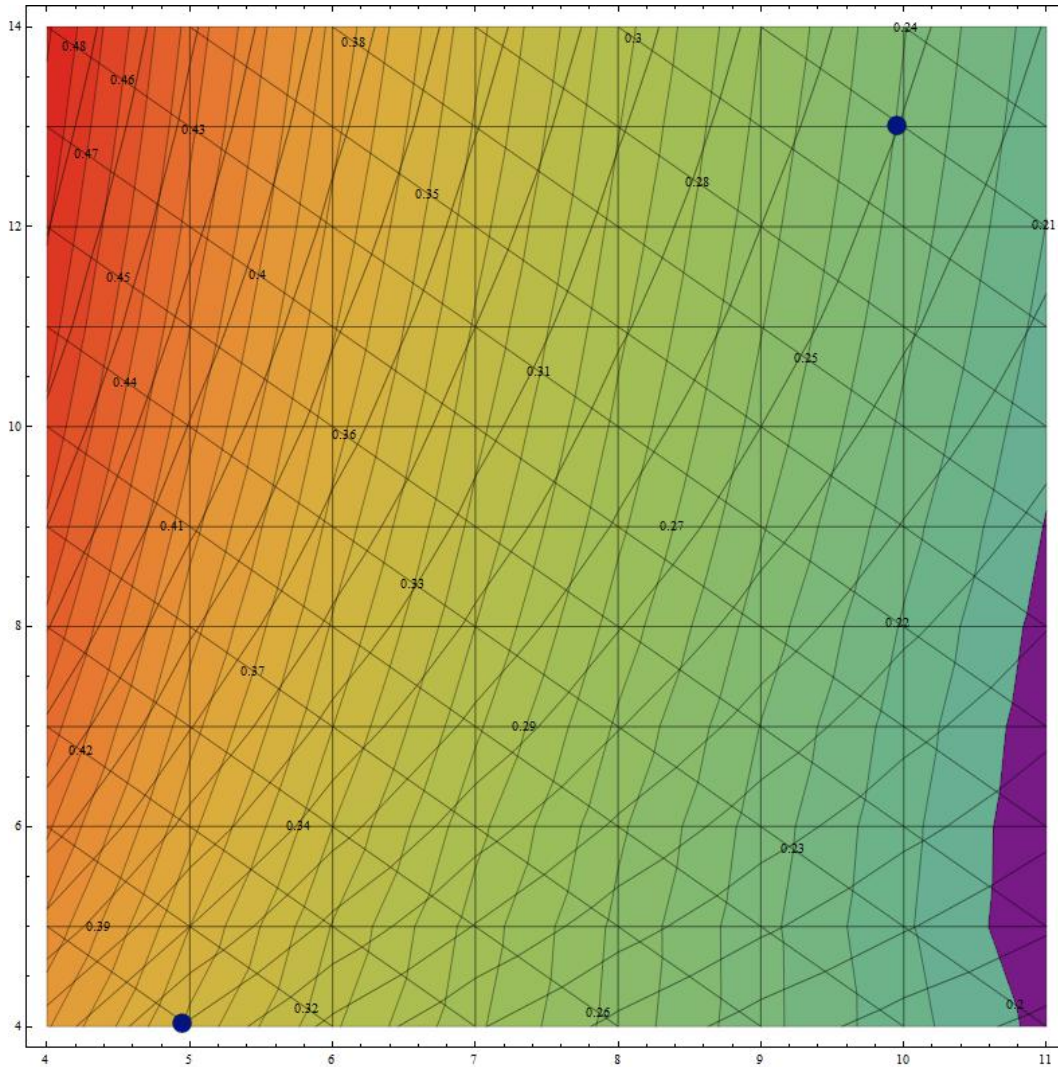


Figure 3-19: SEPM results. Contour lines are plotted for constant conduction band versus constant bandgap. The point (10 ML InAs, 13 ML GaSb) occurs at 0.24eV. A line of constant conduction band is traced to the point (5 ML InAs, 4 ML GaSb) at 0.35eV to ensure that the change in band is entirely over the valence band.

### 3.4.3.3 N-region

The top n-region must be thin in order to minimize absorption and allow for transmittance of desirable wavelengths to the p-type absorber. However, the effective characteristics of a superlattice result from having a thick stack of multiple periods, with

each period being a few nanometers thick. As such, a superlattice structure cannot be utilized for such a thin n-region. Instead, an alloy is employed. Through varying the elemental composition of the alloy, the lattice constant and electronic band structure can be varied. A quaternary compound allows for the decoupling of the lattice constant from the bandgap, enabling these values to be set independently. For a quaternary compound composed of elements A, B, C, and D, the bandgap is approximated by the ternary compound bandgaps, Equation 3.36, which are approximated by the weighted ratio of the binary bandgaps, Equation 3.37, and the non-linear bowing parameter,  $C$ . The affinity levels of a quaternary compound are determined in the same manner.

$$E_{gABCD}(x, y) = \frac{x(1-x)[yE_{gABC}(x) + (1-y)E_{gABD}] + y(1-y)[xE_{gACD}(y) + (1-x)E_{gBCD}(y)]}{x(1-x) + y(1-y)} \quad 3.36$$

$$E_{gABC}(x) = xE_{gAC} + (1-x)E_{gBC} - x(1-x)C_{ABC} \quad 3.37$$

For the n-region of our diode we use a quaternary compound composed of group III gallium and indium and group V arsenic and antimony. This compound has molecular cationic compositional fraction  $x$  of Ga and  $(1-x)$  of In and anionic compositional fraction  $y$  of As and  $(1-y)$  of Sb ( $\text{In}_{1-x}\text{Ga}_x\text{As}_y\text{Sb}_{1-y}$ ). We use a system of equations to solve for  $x$  and  $y$  compositions that allow for a narrow bandgap and a matching affinity level to that of the rest of the diode. The final structure has an  $x$ -composition of 0.13 and  $y$ -composition of 0.59 ( $\text{In}_{0.87}\text{Ga}_{0.13}\text{As}_{0.59}\text{Sb}_{0.41}$ ) yielding a bandgap of 0.248 eV. The barrier height for the minority carrier holes from the n-region is, therefore,  $\sim 100\text{meV}$ .

### 3.4.3.4 Doping Concentration and Degeneracy Check

The barrier will block minority carrier holes from the n-side. If the n-type doping ( $N_D$ ) is much greater than the p-doping ( $N_A$ ), the minority carrier concentration of holes will be insignificant, since  $p_n N_D = n_i^2 = n_p N_A$ , and blocking of the holes will not affect the reverse saturation current. The minority carrier holes will be greater than the minority carrier electrons if the doping of the p-type absorber is much greater than that of the n-side. As such, the p-type doping should be higher than the n-type doping. With the minority carrier holes blocked, the saturation current, Equation 3.38, reduces to Equation 3.39, which can be rewritten as Equation 3.40. As such, the n-type doping ( $N_D$ ) should still be high to reduce the final value of the dark current. We choose doping values of  $1 \times 10^{18} / \text{cm}^3$  and  $5 \times 10^{18} / \text{cm}^3$  for the n-region and p-region, respectively.

$$I_0 = qA \left( \frac{D_n}{L_n} p_n + \frac{D_p}{L_p} n_p \right) \quad 3.38$$

$$I_0 = qA \left( \frac{D_p}{L_p} n_p \right) \quad 3.39$$

$$I_0 = qA n_i^2 \left( \frac{D_p}{N_d L_p} \right) \quad 3.40$$

The intrinsic carrier equation is given by Equation 3.41, where  $N_c$  and  $N_v$  are the effective conduction band and valence band density of states. At high temperatures the intrinsic carrier concentration ( $n_i$ ) is comparable to the net doping level and may wash out the doping. For small bandgap materials, this effect will take hold at a relatively lower temperature and is therefore an issue of concern.

$$n_i = \sqrt{N_c N_v} e^{-\frac{E_g}{2kT}} \quad 3.41$$

Table 3-2 lists acceptable levels of intrinsic carrier concentrations, which must be at least an order of magnitude greater than the doping concentration. A reasonable doping level is between  $10^{14}$  and  $10^{16}$  /cm<sup>3</sup>. As we increase the doping level, we begin to have trade-offs; namely, the material quality begins to decrease creating dislocations or trap states. The carrier mobility also decreases which decreases the diffusion length and carrier collection. At  $10^{19}$ /cm<sup>3</sup>, these effects are exacerbated and the material is rendered inadequate.

	Doping Level (/cm <sup>3</sup> )	Acceptable intrinsic carrier concentration (/cm <sup>3</sup> )
Good	$10^{14}$ - $10^{16}$	$10^{13}$ - $10^{15}$
Trade-offs	$10^{16}$ - $10^{18}$	$10^{15}$ - $10^{17}$
Bad	$10^{19}$	$10^{18}$

Table 3-2: Doping levels and corresponding acceptable intrinsic carrier concentrations

Here we examine a plot of intrinsic carrier concentration versus cut-off wavelength for room temperature operation, Figure 3-20. The regions are color-coded to correspond to acceptable doping concentrations (yellow), trade-off doping concentrations (orange), and unacceptable doping concentrations (red). At an intrinsic carrier concentration of  $10^{17}$ /cm<sup>3</sup>, the cut-off wavelength is  $9.62\mu\text{m}$  (0.12eV). This puts an upper bound on the wavelength we can go to and still have the device operate as an intrinsic device at room temperature. This calculation demonstrates that our device with a cutoff wavelength of  $5\mu\text{m}$  will not have degeneracy issues at room temperature.

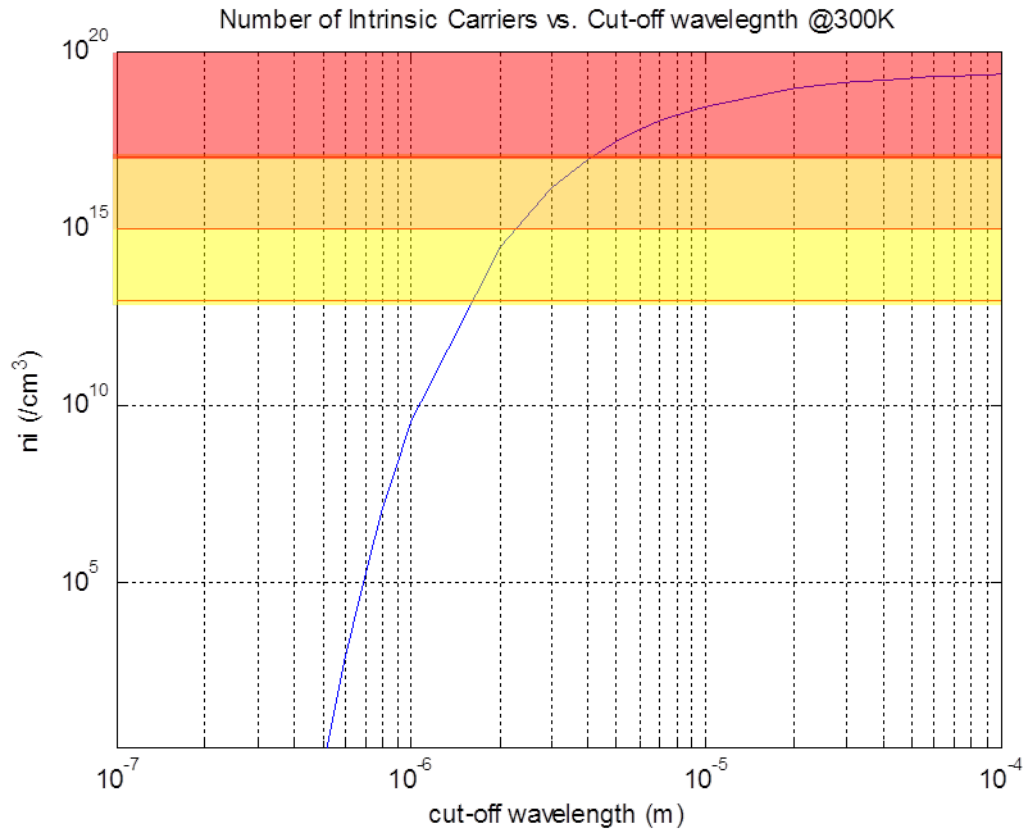


Figure 3-20: Intrinsic carrier concentration versus cut-off wavelength for room temperature operation. The regions are color-coded to correspond to acceptable doping concentrations (yellow), trade-off doping concentrations (orange), and unacceptable doping concentrations (red)

### 3.4.3.5 Band Diagram

The band diagrams for the pin and pBn structures are shown below in Figure 3-21. The conduction band is smooth for both structures, but the pBn has a barrier in the valence band (bottom figure). The bandgap of the n-layer is 0.248 eV and the bandgap of the p-type absorber is 0.24 eV; the barrier has a bandgap of 0.35 eV resulting in a barrier of 100 meV to thermally generated holes from the n-region. The structures both have a 1300nm thick absorption region.

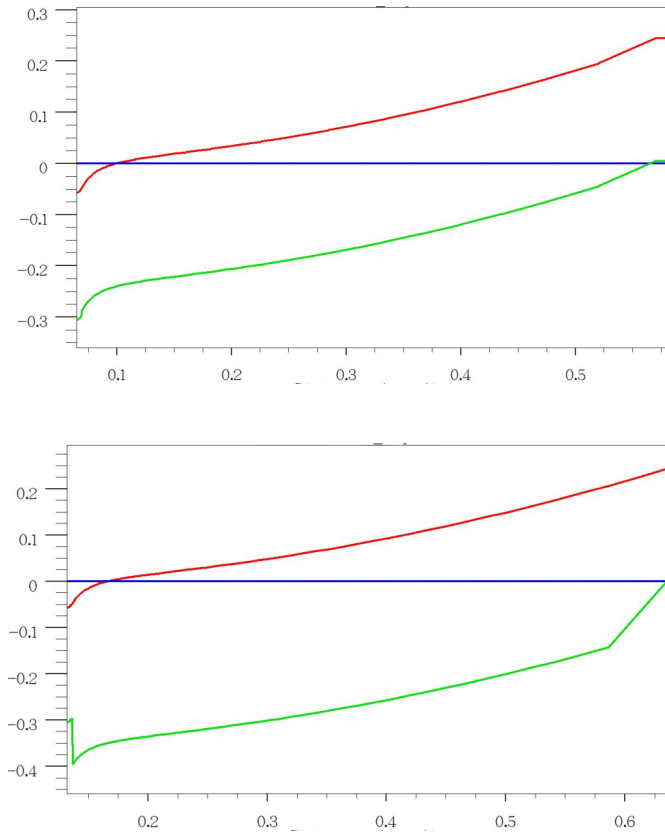


Figure 3-21: Band diagram for InAs/GaSb pin (top) and nBp (bottom) structures (p-region truncated for ease of viewing). The bandgap of the n-layer is 0.248 eV and the bandgap of the p-type absorber is 0.24 eV; the barrier has a bandgap of 0.35 eV resulting in a barrier of 100 meV to thermally generated holes from the n-region. The structures both have a 1300nm thick absorption region. The doping for the n-region and the p-region is  $1 \times 10^{18} / \text{cm}^3$  and  $5 \times 10^{18} / \text{cm}^3$ , respectively.

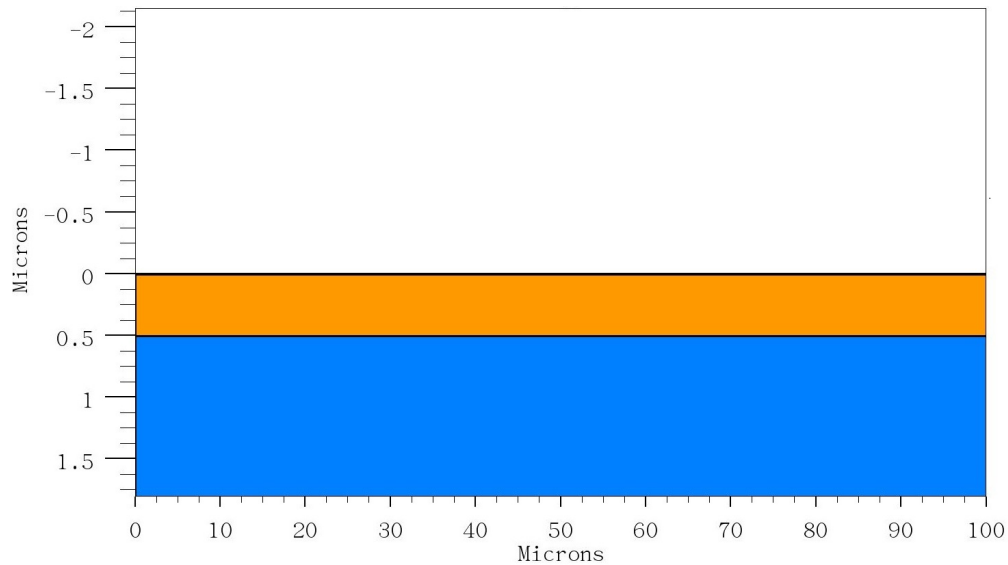


Figure 3-22: Diode stack: The diode is 1.805 microns thick. The intrinsic/barrier region is shown in orange and the p-type absorber region is shown in blue. The n-layer is very thin and is not visible here. The contact is also not visible here: the top contact covers 10% of the surface area.

#### 3.4.3.6 Decrease in Diffusion Current:

##### Calculation:

Here we calculate the reduction in diffusion current when employing a monovalent barrier for InAs/GaSb 5 $\mu\text{m}$  cut-off wavelength devices. For doping concentrations of  $1 \times 10^{18}/\text{cm}^3$  and  $5 \times 10^{18}/\text{cm}^3$  for the n-region and p-region, respectively, we calculate dark currents of  $41.628 \text{ A}/\text{cm}^2$  for the pin structure and  $0.131203 \text{ A}/\text{cm}^2$  for the pBn structure. This is a reduction ratio of approximately 300. The reverse bias pin and pBn dark currents are plotted in Figure 3-23.

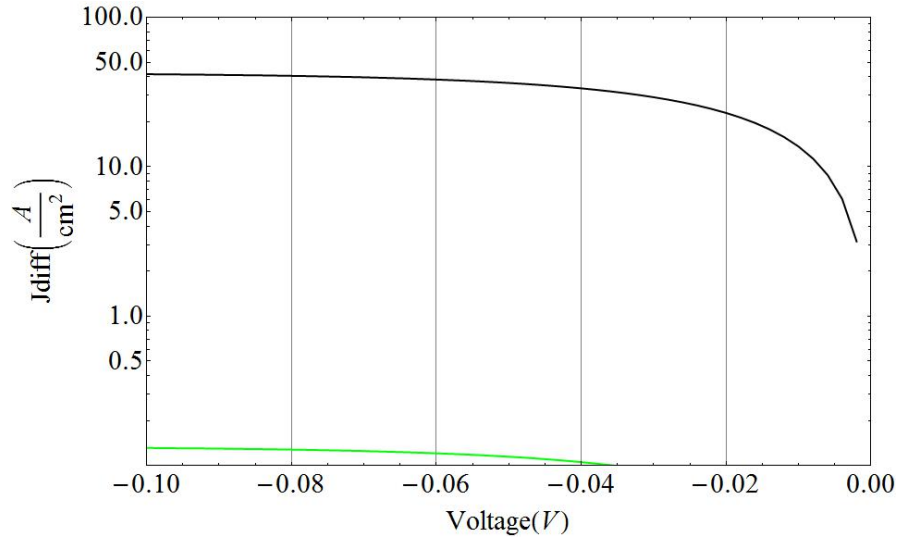


Figure 3-23: Plot of diffusion current versus voltage for pin (black) and pBn (green) for  $N_a=5 \times 10^{18}$  and  $N_D=1 \times 10^{18}$  at room temperature. For a 5  $\mu\text{m}$  cut-off wavelength InAs/GaSb SL photodiode, the pBn diffusion current is reduced by a factor of  $\sim 300$  as compared to the pin diffusion current.

#### *Simulation Results:*

The dark current was also simulated with the program Silvaco. The plot of dark current for the pBn and pin structures at 300K is shown in Figure 3-24. We observe a reduction in the dark current from 17.6  $\text{A/cm}^2$  to 12.24  $\text{A/cm}^2$ , which is a reduction of about one third. The simulation results have lower reduction of dark current than expected, perhaps because these simulations take into account more factors than the dark current equation.

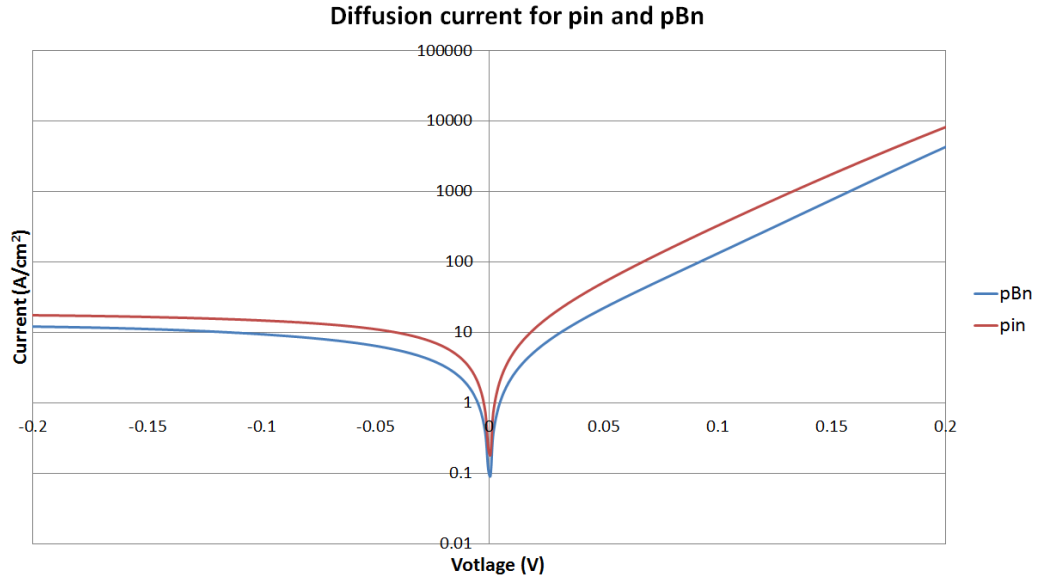


Figure 3-24: Plot of dark current as simulated with Silvaco at 300K showing the reduction in dark current for the pBn over the pin structure.

**3.4.3.7 Open-Circuit Voltage**

The decrease in dark current of the pBn over the pin will lead to an increase in the open-circuit voltage for the pBn, since open-circuit voltage is inversely proportional to the dark current (Equation 3.23). Figure 3-25 shows a plot of the open-circuit voltage of the pin and pBn devices as a function of temperature from simulations with Silvaco. As can be seen from the plot, the pBn structure maintains a higher open-circuit voltage at high temperatures than the pin structure.

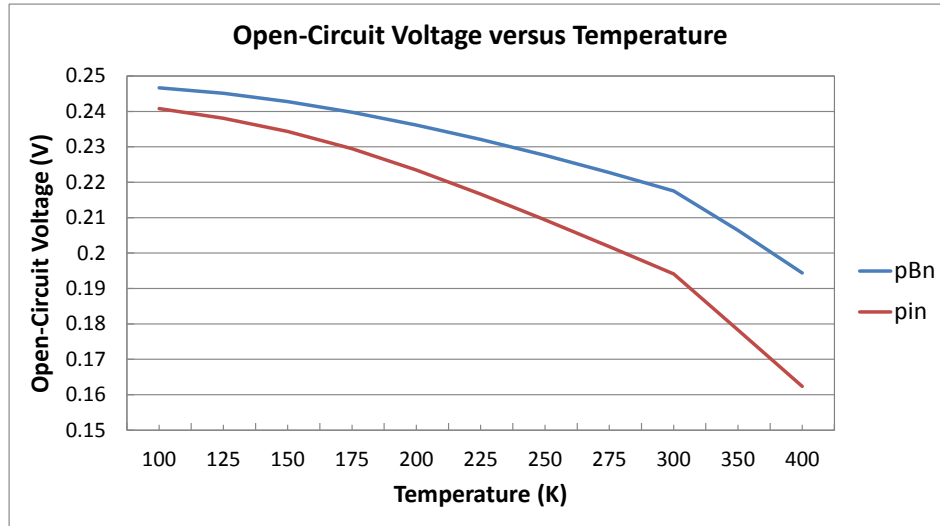


Figure 3-25: Plot of open-circuit voltage versus temperature for the pBn and pin devices. As the temperature increases, the open-circuit voltage of both devices decreases, but the pBn maintains a higher open-circuit voltage as compared to the pin.

#### 3.4.3.8 Photo-generated Current and Efficiency:

For thermophotovoltaic operation, the diode is illuminated with a 1000°C blackbody spectrum. The photogenerated current-voltage resulting for the pin and the pBn structures at 300K are shown in Figure 3-26. The open-circuit voltage improves from 0.19V for the pin to 0.22V for the pBn structure. This improvement in open-circuit voltage leads to an improvement in fill factor from 50.3 for the pin to 53.8 for the pBn and a corresponding 26.5% relative increase in efficiency. Despite the improvement in efficiency, both structures have relatively low nominal efficiencies (0.94% and 1.19% for the pin and pBn respectively). The low efficiency may be due to poor absorption as described in the next section.

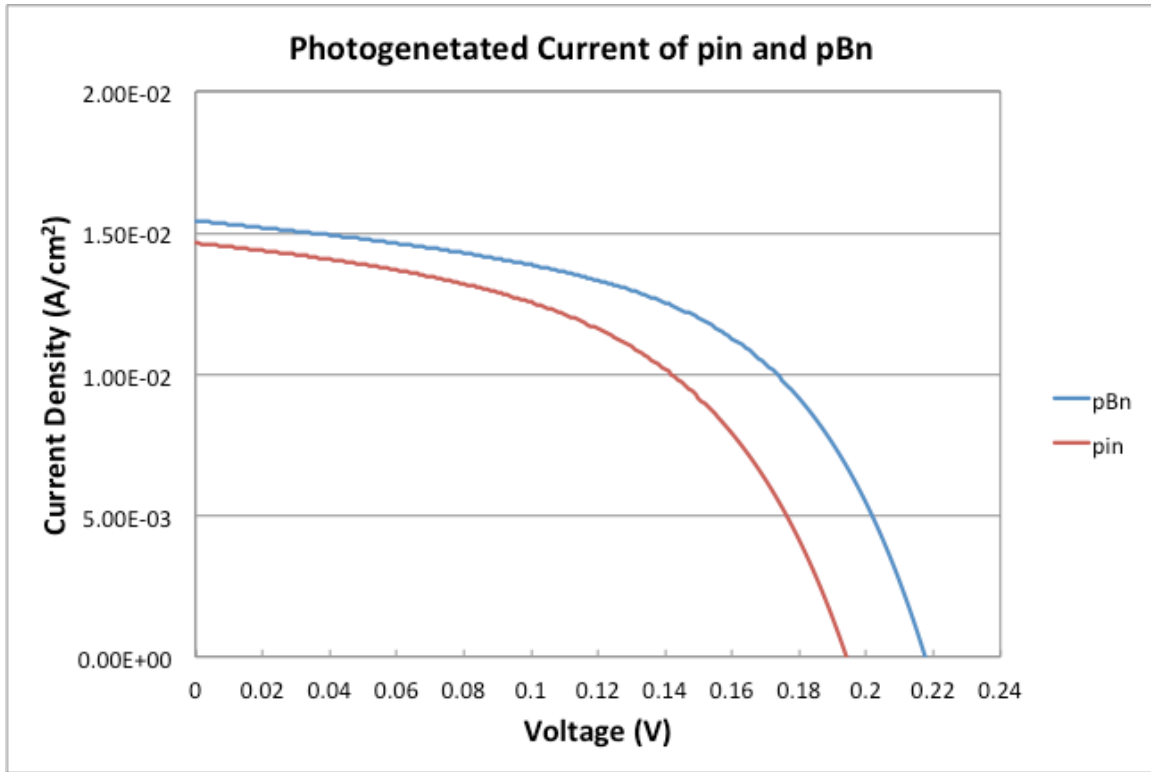


Figure 3-26: Current-voltage curve for pin and pBn under illumination by a 1000°C blackbody spectrum and room temperature operation.

#### 3.4.3.9 Quantum Efficiency:

The quantum efficiency is the probability of generating an electron per incident photon as a function of photon energy. The quantum efficiency can be broken down into the external and internal quantum efficiency (EQE and IQE): the EQE is based on the photon flux *incident* on the diode, whereas the IQE is based on the photon flux that *enters* the diode.

The EQE and IQE of the 5  $\mu\text{m}$  SL TPV barode are shown in Figure 3-27. The quantum efficiency has a maximum of 72% at 0.615  $\mu\text{m}$ . Sub-bandgap photons are rejected as the efficiency approaches zero for increasing wavelengths, as expected. Not all above-bandgap photons, however, are converted, as can be seen by the decreasing efficiency of above-bandgap wavelengths. This decrease in overall conversion efficiency may be due to reflection of light, surface recombination, or shortened diffusion lengths. Methods for improving the conversion efficiency are discussed in Chapter 4.

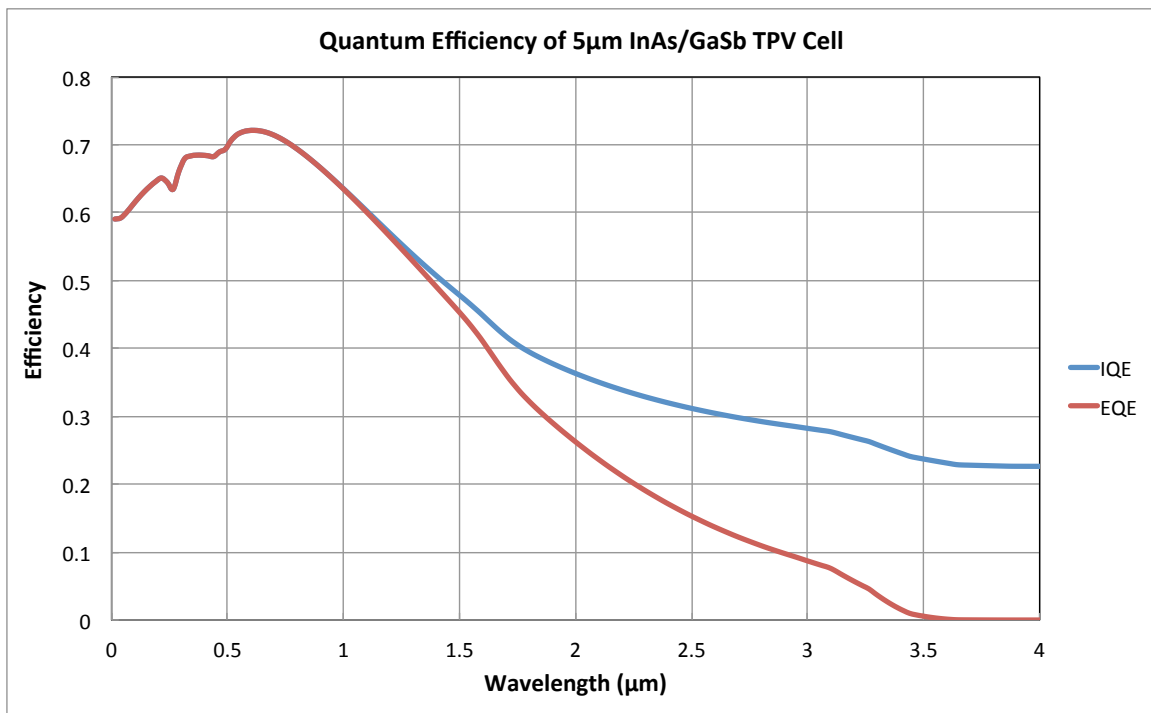


Figure 3-27: Simulated internal and external quantum efficiency of 5  $\mu\text{m}$  TPV photodiode.

#### 3.4.4 Growth, Characterization, and Processing

In the next part of this work, the samples will be grown by molecular beam epitaxy (MBE), a process in which materials are evaporated onto a temperature-controlled substrate in an ultra-high vacuum. The elements incorporated are kept in temperature controlled crucibles and are heated until they sublime. The evaporation of

the materials creates a beam of particles that travel to the surface of the substrate. The substrate is on a block that rotates so that the crystal growth will be uniform. The thickness and composition of the epilayer is controlled by the beam fluxes, which is in turn controlled by the temperature of the crucible.

For growth of III-V materials by MBE, the group-V elements are performed in excess, so it is the flux of the group-III elements that determines the speed of the growth. The temperature of the substrate is critical: it needs to be low enough to allow bonding, but high enough to desorb the group V elements.

During the growth, the samples will be characterized by reflective high energy electron diffraction (RHEED). RHEED can be used to measure the speed of the growth because as each layer is grown the reflectivity changes accordingly. This is used to calibrate the III and V incorporation rates as a function of flux. These values are then used to obtain the flux values for getting the desired growth rates. RHEED can also be used to ensure that the oxide layer has been removed from the sample.

After the samples are grown, they will be characterized with x-ray diffraction (XRD) - a non-destructive process in which x-ray scattering by the sample lattice creates a distinct diffraction pattern. The diffraction spectrum is reported as the reflected intensity versus the detector angle  $\theta$ . When a layer is grown on a substrate, two peaks are observed in the spectra: one for the substrate and one for the layer that is grown. For a superlattice, there will be additionally be satellite peaks. The periodicity of the superlattice is then determined by Bragg's Law (Equation 3.42), with periodicity ( $p$ ), diffraction order ( $n$ ), and angle of diffraction ( $\theta$ ) from x-ray wavelength ( $\lambda$ ). After the material has been characterized, standard photolithography processes will be used to form the metal contacts and fabricate the device.

$$n\lambda = 2p \sin \theta$$

3.42

### 3.5 Chapter Summary

In this chapter we investigated extending the operational wavelength of thermophotovoltaic devices. We proposed extending the cut-off wavelength of TPV diodes to 5  $\mu\text{m}$  (0.25eV) to optimally convert radiation from  $\sim 1,000^\circ\text{C}$  blackbody sources. To ensure that the diode would remain extrinsic during room temperature operation at these wavelengths, we first investigated the degeneracy limit based on doping limitations and found that diodes remain extrinsic at 300K for cut-off wavelengths up to 9.62  $\mu\text{m}$ . As such, our device with a cut-off wavelength of 5 $\mu\text{m}$  will not have degeneracy issues.

In order to establish longer wavelength TPV diodes, we investigated methods of improving the efficiency by reducing the dark current. We proposed that the dark current of a TPV diode may be reduced through incorporation of a monovalent, wide bandgap barrier layer within the PN junction and further through superlattice structuring. We used the SEPM method to design an InAs/GaSb superlattice with a barrier of 100meV in the valence band.

We calculated the reduction in diffusion current when employing a monovalent barrier for InAs/GaSb TPV diodes. At room temperature, employing a wide bandgap

barrier reduces the intrinsic carrier concentration from  $10^{43}/\text{cm}^6$  to  $10^{38}/\text{cm}^6$ , a five order of magnitude difference. This leads to a dramatic reduction in the diffusion current – a calculated reduction of two orders of magnitude.

We first simulated the InAs/GaSb superlattice TPV diode without illumination. We found that the dark current was indeed reduced for the pBn structure. We then studied the TPV diode under illumination of a  $1,000^\circ\text{C}$  blackbody spectrum with and without the barrier at room temperature. We expected that the decrease in dark current of the pBn would lead to an increase in the open-circuit voltage, since the open-circuit voltage is inversely proportional to the dark current. We observed that the open-circuit voltage improved from 0.194 V for the pin to 0.218 V for the pBn structure. This improvement in open-circuit voltage leads to an improvement in fill factor from 50.3 for the pin to 53.8 for the pBn. The resulting efficiency increases from 0.94% to 1.19%, a relative increase in efficiency of 26.5%. We conclude that the InAs/GaSb pBn diode is a good potential device candidate for longer wavelength thermophotovoltaics as it improves the overall efficiency as compared to the traditional pin structure.

## 4 System Efficiency

### 4.1 System Efficiency Calculations

The conversion efficiency of the system as a whole is determined by the product of the following terms: the chemical to radiation efficiency  $\eta_{CR}$ , the emitter to TPV cell view factor ( $VF$ ), and the TPV diode conversion efficiency  $\eta_{TPV}$  (Equation 4.1) [9].

$$\eta = \eta_{CR} * VF * \eta_{TPV} \quad 4.1$$

#### 4.1.1 Chemical to Radiation Efficiency

For a combustion temperature of 550°C and highly thermally conductive walls, we can approximate the emitter temperature as 550°C. For this emitter temperature the emissive power density is calculated by Equation 4.3 and is 2.6 W/cm<sup>2</sup>. For the emitter surface area of 42.25 cm<sup>2</sup>, this yields a total radiated power of ~110 Watts. From Section 2.4.1, the total maximum theoretical power generation from the fuel is 1kW. As such, the overall chemical to radiation efficiency is 11%.

$$e_b(\lambda, T)d\lambda = \frac{2\pi hc^2 d\lambda}{\lambda^5 (e^{hc/\lambda kT} - 1)} \quad 4.2$$

$$\int_0^\infty e_b(\lambda, T)d\lambda = \frac{2\pi^5 k^4}{15h^3 c^2} T^4 = \sigma_{sb} T^4 \quad 4.3$$

### 4.1.2 View Factor

View factor is given by the fraction of radiation incident on the cells from the total radiation from the emitter. For a coaxial square plate configuration with plates of length  $L$  separated by distance  $D$ , the view factor from plate 1 to plate 2 ( $F_{12}$ ) can be calculated by Equations 4.4-4.9 [55]. An emitter plate of 6.35 cm in length and plate to cell separation of 5 mm results in a view factor 0.86.

$$F_{12} = \frac{(A + B + C)}{\pi \left(\frac{L_1}{D}\right)^2} \quad 4.4$$

$$A = \ln \frac{\left[\left(\frac{L_1}{D}\right)^2 \left(1 + \left(\frac{L_2}{L_1}\right)^2 + 2\right)\right]^2}{(y^2 + 2)(x^2 + 2)} \quad 4.5$$

$$B = \sqrt{y^2 + 4} \left[ \left( y \tan^{-1} \frac{y}{\sqrt{y^2 + 4}} \right) - \left( x \tan^{-1} \frac{x}{\sqrt{y^2 + 4}} \right) \right] \quad 4.6$$

$$C = \sqrt{x^2 + 4} \left[ \left( x \tan^{-1} \frac{x}{\sqrt{x^2 + 4}} \right) - \left( y \tan^{-1} \frac{y}{\sqrt{x^2 + 4}} \right) \right] \quad 4.7$$

$$x = \frac{L_1}{D} \left( 1 + \frac{L_2}{L_1} \right) \quad 4.8$$

$$y = \frac{L_1}{D} \left( 1 - \frac{L_2}{L_1} \right) \quad 4.9$$

### 4.1.3 TPV Cell Conversion Efficiency

The cell conversion efficiency is the ratio of converted radiation to the total incident radiation upon the cell (Equation 4.10). The converted spectrum is found by integrating the product of the quantum efficiency, as discussed in 3.4.3.9, and the incident spectrum (Equation 4.11). Figure 4-1 shows the incident spectrum (blue curve) on the TPV diode and the external quantum efficiency (red curve) of the TPV diode. The product of these two curves is shown in green and represents the amount of radiation

that is actually converted by the TPV diode. The ratio of the area under the green curve to the area under the blue curve yields a TPV cell conversion efficiency of 2.85%.

$$\eta_{TPV} = \frac{\text{Converted Radiation}}{\text{Total Incident Radiation}} \quad 4.10$$

$$\text{Converted Spectrum} = \int_0^{\infty} QE * \text{Incident Radiation}(\lambda) \quad 4.11$$

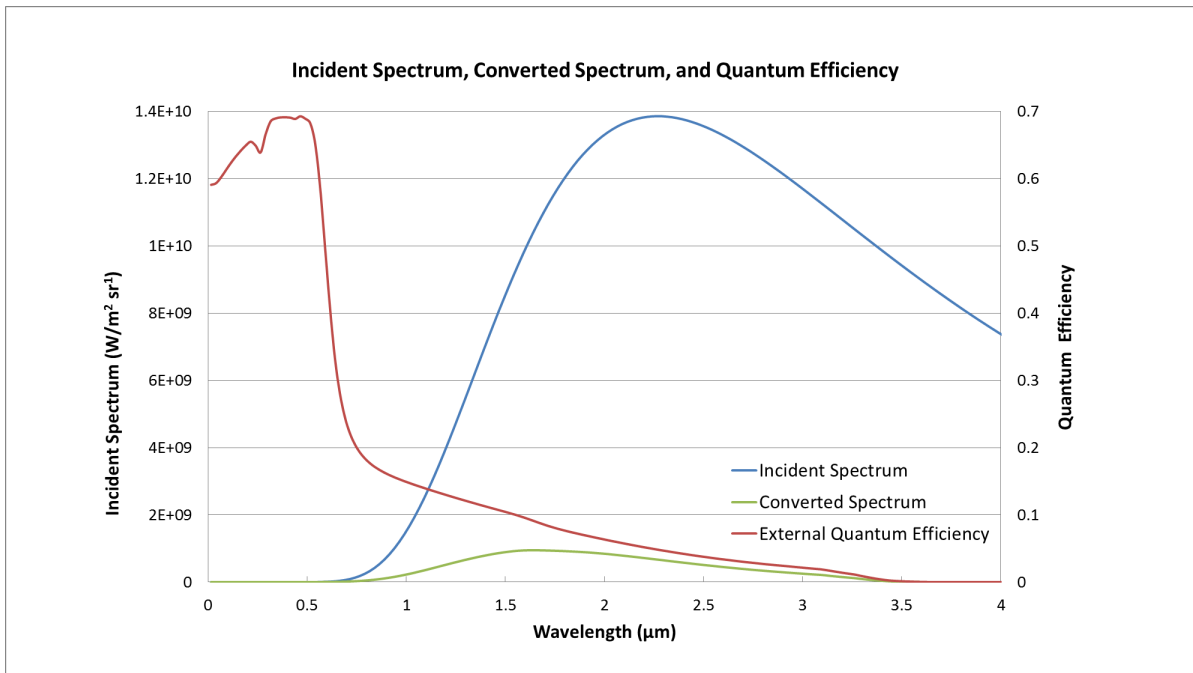


Figure 4-1: Incident spectrum (blue), converted spectrum (green), and quantum efficiency (red)

#### 4.1.4 Total System Efficiency

As discussed previously, the total system conversion efficiency is given by the product of the chemical to radiation efficiency, the emitter to TPV cell view factor ( $VF$ ), and the TPV cell efficiency as in Equation 4.1 [9]. For a chemical to radiation efficiency

of 11%, a view factor of 86%, and a TPV cell efficiency of 2.85%, the total system efficiency is 2.70%.

## 4.2 Improving System Efficiency

The overall system efficiency can be increased by improving the efficiencies of the combustor, the cavity, and the TPV cell, as detailed in the following sections.

### 4.2.1 Stabilizing the Combustion Reaction and Reducing Heat Losses

As calculated in the previous section, only 11% of the power from the fuel is transferred to emitter radiation. For a combustion temperature of 550°C, the reactor is far from the maximum possible combustion temperature as calculated in Section 2.4.1. The combustion reaction can be improved through further treatments of the catalyst surface and through mitigating heat losses. For the heat that is generated, the majority is lost to the surrounding environment. Heat loss is given by the sum from all contributions: forced convective loss as the hot exhaust gas is pushed out of the chamber, radiative heat loss from photons not radiant upon the energy converter, free convective heat loss as heat rises from the combustor, and conductive heat loss across the combustor walls not aligned with the TPV cells (4.12). The heat loss mechanisms are described in more detail in the following sections, as well as avenues for mitigating these losses.

$$q_{loss} = q_{exhaust} + q_{rad} + q_{conv} + q_{cond} \quad 4.12$$

#### 4.2.1.1 Exhaust Heat Loss

The energy of the exhaust loss (Equation 4.13) is proportional to the specific heat capacity ( $c$ ) [kJ/kg\*K], the flow rate ( $\dot{m}$ ) [kg/s], and the difference between the temperature of the combustor ( $T_c$ ) and the ambient temperature ( $T_a$ ). For the temperature of our combustor this is approximately 6 Watts. The exhaust heat loss can be decreased by recirculating the hot exhaust to pre-heat the reactants in “excess enthalpy” burners. Heat recuperation techniques have proven to increase the emitter wall temperature and establish more uniform thermal radiation along the emitter walls [19], [56], [57].

$$q_{exhaust} = c\dot{m}(T_c - T_a) \quad 4.13$$

#### 4.2.1.2 Radiative Heat Loss

The radiative heat loss comes from the surface area of the combustor walls not aligned with the TPV cells. The radiative heat loss is given by the Stefan-Boltzmann Law (Equation 4.14) and is proportional to the emissivity ( $\epsilon$ ), the Stefan Boltzmann constant ( $\sigma$ ), the wall temperature ( $T$ ), and the surface area ( $A$ ). These losses can be reduced by placing cells on the non-radiating sides or using a thinner stack.

$$q_{rad} = \epsilon\sigma T_{wall}^4 \sum A \quad 4.14$$

#### 4.2.1.3 Conduction Loss

Conduction occurs if there is a temperature gradient within a solid. Fourier's Law (Equation 4.15) expresses the conductive heat transfer in terms of the thermal conductivity ( $k$ ) [W/m K], heat transfer area ( $A$ ), material thickness ( $t$ ), and temperature difference across the material. This is usually <1W and is considered negligible.

$$q_{cond} = \frac{\Delta T k A}{t} \quad 4.15$$

#### 4.2.1.4 Convective Heat Loss

If the combustor is operated in ambient conditions, heat will be transferred by natural convection according to Newton's Law of Cooling, Equation 4.16, where  $h$  is the convection coefficient. This heat loss can be eliminated by operation in vacuum.

$$q_{convection} = h(T_c - T_a) \sum A \quad 4.16$$

### 4.2.2 Incorporating Spectral Control

The optimal efficiency of a photovoltaic diode for an incident spectrum was determined by Shockley and Queisser [42]. The efficiency is written in terms of the dimensionless bandgap parameter,  $u_g$ , which is the ratio of the bandgap energy ( $E_g$ ) to the thermal energy ( $kT$ ) of the emitter (Equations 4.17 and 4.18). Shockley and Queisser showed that a maximum conversion efficiency of 44% occurs for a bandgap parameter value of 2.17. However, if spectral control is introduced to modify the incident spectrum, the spectrum can be better matched to the TPV cell and the theoretical maximum efficiency increases. Assuming an emissivity of zero for below bandgap

photons and an emissivity of one for above bandgaps photons, the efficiency can be re-written as Equation 4.19 [41]. For a bandgap of 0.24 eV and emitter temperature of 1,000°C, the incorporation of spectral control increases the maximum efficiency temperature from 44% to 56%.

$$\eta = \frac{15}{\pi^4} u_g \int_{u_g}^{\infty} \frac{u^2}{e^u - 1} du \quad 4.17$$

$$u_g = \frac{E_G}{kT} \quad 4.18$$

$$\eta_{max} = u_g \frac{\int_{u_g}^{\infty} \frac{u^2}{e^u - 1} du}{\int_{u_g}^{\infty} \frac{u^3}{e^u - 1} du} \quad 4.19$$

As the value of the bandgap parameter increases, the efficiency approaches 100%. However, it should be noted that as the bandgap parameter increases, either the emitter temperature must approach zero or the bandgap must approach infinity. Thus for an ideal system, as the efficiency approaches 100%, the power vanishes. In using spectral control to improve the efficiency there is therefore a tradeoff with output power. For example, a lower temperature emitter of 500°C increases the efficiency from 56% to 70%, but decreases the power density from 6.5 W/cm<sup>2</sup> to 0.8 W/cm<sup>2</sup>.

### 4.2.3 Improving TPV Cell Efficiency

For an emitter temperature of 1,000°C, with an emitter surface area of ~40 cm<sup>2</sup> and a power density of 6.5 W/cm<sup>2</sup>, this design has the potential to generate 260 Watts.

Given the view factor of 86%, this value is reduced to 223.6 Watts. This is the maximum power that would be generated if the cell had a conversion efficiency of 100%. However, the conversion efficiency of the TPV cell was much lower than this value. Given the simulated cell conversion efficiency and the maximum incident wattage, the system can only generate 6.37 Watts. In order to reach the 50 W goal, the cell efficiency would have to increase to 22%. This value is reasonable considering present PV efficiencies achieved today. That being said, the InAs/GaSb SL TPV cell efficiency is far from this mark. More work is to be done to increase the TPV cell efficiency to 22%. For example, by adding a back surface reflector, photons not absorbed on the first pass can have a second attempt at absorption. Additionally, by incorporating anti-reflection coatings, the radiation lost to reflection can be transmitted.

### **4.3 Chapter Summary**

In this chapter, the total system efficiency of the TPV-CFR system was calculated. The chemical to radiation efficiency of the combustor was 11%, the view factor was 86%, and the TPV spectral efficiency was 2.85%, leading to an overall system efficiency of 2.70%. The overall system efficiency can be increased by improving the individual efficiencies of the combustor, the cavity, and the TPV cell. Various methods of improving these efficiencies were discussed.

To improve the combustion system efficiency, the most important factor is to reduce heat losses. These heat losses cause the reaction to extinguish and combustion is not sustainable. The majority of heat is lost to free convection as the hot air is pushed out through the exhaust and into the atmosphere. The exhaust heat losses can be mitigated by recirculating the exhaust to preheat the incoming fuel-air mixture, or by

using additional TPV cells to absorb the waste heat from the exhaust. As such, waste heat recycling will be included in the second iteration of this design. Additionally, the efficiency of the cavity can be improved by including a selective emitter instead of a broadband emitter. For example, the theoretical maximum TPV cell efficiency increases by more than 10% when using a selective emitter for a TPV diode with bandgap of 0.24 eV and emitter temperature of 1,000°C. Finally, the TPV cell efficiency itself can be improved by increasing absorption with anti-reflection coatings and back surface reflectors.

## **5 Thesis Summary**

In this thesis we presented the design and implementation of a meso-scale catalytic flow reactor (CFR) for powering thermophotovoltaic (TPV) devices for portable power generation applications. The power output goal was 50 Watts and the system was designed to meet this need. The first part of this thesis was the design, construction, and testing of the catalytic flow reactor. The CFR was fueled by a fuel-lean mixture with an air to propane molar ratio of 6:1. The reactor incorporated a platinum-plated nickel catalyst to lower the activation energy and therefore the auto-ignition temperature. The system was heated externally and ignition occurred when the catalyst reached a temperature of 285.7°C, as opposed to the non-catalytic auto-ignition temperature of 540°C. Combustion was indicated by a 263°C jump in temperature over the course of five seconds, with the reaction peaking at 550°C. This relatively low combustion temperature resulted in a combustion efficiency of only 7.4%. Moreover, catalytic combustion was not repeatable in a consistent manner. Surface analysis of the

catalyst by XPS revealed that post-combustion the catalyst was covered by a nickel oxide film. It was hypothesized that removing this oxide layer would improve the combustion reaction. A surface treatment was developed to remove the nickel oxide by heating the catalyst and subsequently reducing the catalyst surface in a hydrogen environment for eight hours. The catalyst surface was examined post-treatment to reveal that the oxide was partially removed to reveal 30% platinum content. These samples underwent testing and did not yield successful combustion, however. It was concluded that further surface treatment techniques must be developed to fully uncover the 70% platinum content in the bulk of the catalyst. Additionally, measures must be introduced to mitigate heat losses to help sustain the combustion reaction.

The second stage of this research project was designing longer wavelength TPV diodes to optimally convert thermal radiation from the CFR. In order to extend the operational wavelength of TPV, we investigated methods of reducing the parasitic dark currents that plague short-bandgap diodes. We proposed that the dark current of a TPV diode may be reduced through incorporation of a monovalent, wide bandgap barrier layer within the PN junction and further through superlattice structuring. We used the SEPM method to design an InAs/GaSb superlattice with a smooth conduction band and a barrier of 100 meV in the valence band. We calculated the reduction in diffusion current while employing a monovalent barrier for InAs/GaSb TPV diodes. At room temperature, employing a wide bandgap barrier reduces the intrinsic carrier concentration from  $10^{43}/\text{cm}^6$  to  $10^{38}/\text{cm}^6$ . This decrease in intrinsic carrier concentration leads to a large reduction in the diffusion current – an estimated reduction of two orders of magnitude.

We simulated the InAs/GaSb superlattice TPV diode using the program Silvaco. We found that the dark current was indeed reduced for the pBn structure. The decrease in dark current of the pBn over the pin leads to an increase in the open-circuit voltage for the pBn since the open-circuit voltage is inversely proportional to the dark current. We studied the InAs/GaSb TPV diode under illumination of a 1,000°C blackbody spectrum with and without the barrier at room temperature. We found that the open-circuit voltage increases from 0.194 V for the pin to 0.218 V for the pBn structure. This increase in open-circuit voltage leads to an improvement in fill factor from 50.3 for the pin to 53.8 for the pBn. The diode efficiency therefore increases from 0.94% to 1.19%, a relative improvement of 26.5%. This improvement allows the pBn diode to achieve the same efficiency at 300K that the pin would normally achieve at 225K, thus allowing for an increase in operation temperature. We conclude that the InAs/GaSb pBn diode is a good device candidate for long wavelength thermophotovoltaics as it will enable longer wavelength devices to operate more efficiently at the desired temperatures.

Finally, we investigated the degeneracy limit for room temperature operation based on doping limitations and found that devices can operate with cut-off wavelengths up to 9.62  $\mu\text{m}$  and remain extrinsic. This means that TPV diodes can be designed to convert waste heat from temperature sources as low as 500°C without becoming intrinsic, enabling further device applications.

The total system efficiency of the TPV-CFR was 2.70%, or 1.15% if the series and shunt resistances of the diode are accounted for. The system efficiency can be increased by improving the individual component efficiencies. To improve the combustion efficiency, in addition to further catalyst development, heat losses must be reduced, since loss of heat forces the reaction to extinguish. The majority of heat is lost

as the hot air is pushed out through the exhaust and into the atmosphere. The exhaust heat losses can be mitigated by recirculating the hot exhaust to preheat the incoming fuel-air mixture. As such, heat recycling will be included in the second iteration of this design. In addition to improving the combustion efficiency, the cavity and TPV cell efficiency can also be improved by including a selective emitter. For example, the theoretical maximum TPV cell efficiency increases by more than 10% when using a selective emitter for a diode with bandgap of 0.24 eV and emitter temperature of 1,000°C. Finally, the TPV cell efficiency can further be improved by including features such as anti-reflection coatings and back surface reflectors. If the TPV cell efficiency can be increased to 22% and the combustion efficiency is increased so that the emitter can reach a temperature of 1,000°C, the system will be able to generate 50 watts. While the present system is far from this mark, typical photovoltaic cell efficiencies exceed 20%, so with further system optimization this goal is feasible.

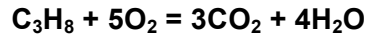
## Appendix

### A. Catalyst Recipe

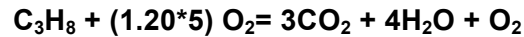
This recipe is from Dr. Jay Peck.

- Weigh samples
- Clean the nickel substrates ultrasonically.
- Dissolve 2g dihydrogen hexachloroplatinate(IV) salt ( $\text{H}_2\text{PtCl}_6\text{-6H}_2\text{O}$ ) into 16mL de-ionized water to make 12.5% platinum solution.
- Submerge the nickel substrates in the solution for 10 minutes.
- Dry the substrates in a furnace with reducing environment. Run  $\text{N}_2$  at 100°C for 2 hours to remove water. Run  $\text{H}_2$  at 300°C for 2 hours to remove Cl.
- Weigh samples

## B. Mass Flow Rate Calculations



The reaction for oxygen and propane yields a 5:1 molar ratio. However, we will use excess air, or a fuel-lean mixture to ensure efficiency (if not enough air is fed to the combustor, unburned fuel, soot, smoke, and carbon monoxide may result in the exhaust - this lowers combustion efficiency). With 20% excess air, the stoichiometry has a 6:1 air to propane molar ratio:



The energy density of propane is 46kJ/g. To generate 50W, assuming a 5% overall system efficiency, we will aim to generate 1kW. For 1kW the required mass flow of the propane/air mixture is then  $1,000\text{J/s} / 46,000\text{J/g} = 0.022 \text{ g/s} = 22 \text{ mg/s}$ . This corresponds to an air flow rate of:

$$\frac{.022\text{g (C}_3\text{H}_8\text{+Air)}}{\text{s}} * \frac{1 \text{ packet of reactants}}{6 \cdot 28.9 + 1 \cdot 44 \text{ (g C}_3\text{H}_8 + \text{Air)}} * \frac{6 \text{ mol Air}}{1 \text{ packet reactants}} * \frac{28.9 \text{ g Air}}{1 \text{ mol Air}} = 17.5 \text{ mg/s}$$

And a propane flow rate of:

$$\frac{.022\text{g (C}_3\text{H}_8 + \text{Air)}}{\text{s}} * \frac{1 \text{ packet of reactants}}{6 \cdot 28.9 + 1 \cdot 44 \text{ (g C}_3\text{H}_8 + \text{Air)}} * \frac{1 \text{ mol C}_3\text{H}_8}{1 \text{ packet reactants}} * \frac{44 \text{ g C}_3\text{H}_8}{1 \text{ mol C}_3\text{H}_8} = 4.5 \text{ mg/s}$$

## REFERENCES

- [1] D. C. Walther and J. Ahn, "Advances and challenges in the development of power-generation systems at small scales," *Progress in Energy and Combustion Science*, vol. 37, no. 5, pp. 583-610, Sep. 2011.
- [2] F. Weinberg, "The first halfmillion years of combustion research and today's burning problems," in *15th Int. Symposium on Combustion*, 1974.
- [3] DOE, "Comparison of Fuel Cell Technologies." [Online]. Available: <http://energy.gov/eere/fuelcells/types-fuel-cells>. [Accessed: 12-Aug-2014].
- [4] A. Mitsos and P. Barton, *Microfabricated Power Generation Devices: Design and Technology*. 2009.
- [5] S. Energy, "Jenny ND Terra." .
- [6] G. Guazzoni and S. Matthews, "A Retrospective of Four Decades of Military Interest in Thermophotovoltaics," in *6th International Conference on Thermophotovoltaic Generation of Electricity*, 2004.
- [7] E. Doyle, F. Becker, K. Shukla, and L. Fraas, "Design of a TPV Battery Substitute," in *AIP 460, 4th TPV Conference*, 1999.
- [8] E. Doyle, K. Shukla, and M. Metcalfe, "Development and Demonstration of a 25W TPV Power Source for a Hybrid Power System," 2001.
- [9] L. Fraas and J. Avery, "Design of a Portable Fuel Fired Cylindrical TPV Battery Replacement," in *AIAA 9th International Energy Conversion Engineering Conference*, 2011.
- [10] D. G. Norton and D. G. Vlachos, "A CFD Study of Premixed Methane/Air Mixtures," *Combustion Flame*, vol. 138, pp. 97-107, 2004.
- [11] L. Sitzki, K. Borer, E. Schuster, P. D. Ronney, and S. Wussow, "Combustion in Microscale Heat-Recirculating Burners," 2001, pp. 1-4.
- [12] D. G. Norton and D. G. Vlachos, "Hydrogen assisted self-ignition of propane/air mixtures in catalytic microburners," *Proceedings of the Combustion Institute*, vol. 30, no. 2, pp. 2473-2480, Jan. 2005.

- [13] P. Aghalayam, P.-A. Bui, and D. G. Vlachos, "The role of radical wall quenching in flame stability and wall heat flux: hydrogen-air mixtures," *Combust. Theory Model.*, vol. 2, pp. 515–530, 1998.
- [14] A. Linan and F. A. Williams, *Fundamental Aspects of Combustion*. New York: Oxford University Press, 1993.
- [15] C. M. Miesse, R. I. Masel, C. D. Jensen, M. A. Shannon, and M. Short, "Submillimeter- scale combustion," *AIChE J.*, vol. 50, pp. 3206–3214, 2004.
- [16] W. M. Yang, S. K. Chou, C. Shu, Z. W. Li, and H. Xue, "A prototype microthermophotovoltaic power generator," *Applied Physics Letters*, vol. 84, no. 19, p. 3864, 2004.
- [17] O. M. Nielsen, L. R. Arana, C. D. Baertsch, K. F. Jensen, and M. a. Schmidt, "A thermophotovoltaic micro-generator for portable power applications," *TRANSDUCERS '03. 12th International Conference on Solid-State Sensors, Actuators and Microsystems. Digest of Technical Papers (Cat. No.03TH8664)*, vol. 1, pp. 714-717, 2003.
- [18] W. Chan et al., "2010\_CHAN\_High\_Ecciciency\_MM\_scale\_TPV\_generator\_TPV9," in *TPV-9*, 2010.
- [19] W. M. Yang, J. J. Chua, J. F. Pan, D. Y. lang, and H. An, "Development of micro-thermophotovoltaic power generator with heat recuperation," *Energry Conversion and Management*, vol. 78, pp. 81-87, 2014.
- [20] J. Ahn, C. Eastwood, L. Sitzki, and P. D. Ronney, "Gas-phase and catalytic combustion in heat-recirculating burners," *Proceedings of the Combustion Institute*, vol. 30, pp. 1-29, 2004.
- [21] G. Neuer, "Spectral and Total Emissivity Measurements of Highly Emitting Materials," *International Journal of Thermophysics*, vol. 16, no. 1, pp. 257-265, 1995.
- [22] D. Goodwin, "Cantera." [Online]. Available: <http://code.google.com/p/cantera/>.
- [23] G. Vesper and L. D. Schmidt, "Ignition and extinction in the catalytic oxidation of hydrocarbons over platinum," *AIChE Journal*, vol. 42, no. 4, pp. 1077-1087, Apr. 1996.
- [24] V. Seshadri and N. S. Kaisare, "Ignition strategies for fuel mixtures in catalytic microburners," *Combustion Theory and Modelling*, vol. 14, no. 1, pp. 23-40, Mar. 2010.

- [25] N. S. Kaisare, G. D. Stefanidis, and D. G. Vlachos, "Comparison of ignition strategies for catalytic microburners," *Proceedings of the Combustion Institute*, vol. 32, no. 2, pp. 3027-3034, 2009.
- [26] M. W. Dashiell et al., "Quaternary InGaAsSb Thermophotovoltaic Diodes," *IEEE Transactions on Electron Devices*, vol. 53, no. 12, pp. 2879-2891, Dec. 2006.
- [27] H. Mohseni, V. Litvinov, and M. Razeghi, "Interface-induced suppression of the Auger recombination in type-II InAs/GaSb superlattices," *Physical Review B*, vol. 58, no. 23, pp. 15378-15380, Dec. 1998.
- [28] H. Kolm, "Solar-battery power source Quarterly Progress Report Solid State Research, Group 35," Lexington, MA: MIT Lincoln Laboratory, 1956.
- [29] B. Bitnar, "Silicon, germanium and silicon/germanium photocells for thermophotovoltaics applications," *Semicond Sci Technol*, vol. 18, pp. 221-227, 2003.
- [30] T. Bauer, *Thermophotovoltaics: Basic Principles and Critical Aspects of System Design*. Springer, 2011.
- [31] M. A. Green, K. Emery, Y. Hishikawa, W. Warta, and E. D. Dunlop, "Solar cell efficiency tables (version 39)," *Progress in Photovoltaics: Research and Applications*, vol. 20, no. 1, pp. 12-20, Jan. 2012.
- [32] M. G. Mauk and V. M. Andreev, "GaSb-related materials for TPV cells," *Semiconductor Science and Technology*, vol. 18, no. 5, p. S191-S201, May 2003.
- [33] L. M. Fraas, H. X. Huang, S. Z. Ye, S. Hui, A. J., and B. R., "No Title," in *3rd REL Conf. on the the Thermophotovoltaic Generation of Electricity*, 1997, pp. 33-40.
- [34] E. V. Kunitsyna et al., "Narrow gap III-V materials for infrared photodiodes and thermophotovoltaic cells," *Optical Materials*, vol. 32, no. 12, pp. 1573-1577, Oct. 2010.
- [35] J. T. South et al., "Al<sub>x</sub>Ga<sub>1-x</sub>Sb window layers for InGaAsSb/GaSb thermophotovoltaic cells," 1999, pp. 545-554.
- [36] a. P. Astakhova et al., "Long-wavelength photodiodes based on n-GaSb/n-GaInAsSb/p-AlGaAsSb heterostructures," *Technical Physics Letters*, vol. 33, no. 1, pp. 11-13, Jan. 2007.

- [37] E. V. Kunitsyna et al., "Narrow gap III–V materials for infrared photodiodes and thermophotovoltaic cells," *Optical Materials*, vol. 32, no. 12, pp. 1573-1577, Oct. 2010.
- [38] V. a. Gevorkyan et al., "The Growth of Low Band-Gap InAsSbP Based Diode Heterostructures for Thermo-Photovoltaic Application," *AIP Conference Proceedings*, vol. 890, no. 2007, pp. 165-173, 2007.
- [39] K. J. Cheetham, P. J. Carrington, N. B. Cook, and A. Krier, "Solar Energy Materials & Solar Cells Low bandgap GaInAsSbP pentanary thermophotovoltaic diodes," *Solar Energy Materials and Solar Cells*, vol. 95, no. 2, pp. 534-537, 2011.
- [40] G. D. Cody, "Theoretical maximum efficiencies for thermophotovoltaic devices," vol. 58, no. 1, pp. 58-67, 1999.
- [41] D. L. Chubb, *Fundamentals of Thermophotovoltaic Energy Conversion*. Amsterdam, Netherlands: Elsevier, 2007, p. 515.
- [42] W. Shockley and H. Queisser, "Detailed Balance Limi of Efficiency of p-n Junction Solar Cells," *Jounrla of APplied Physics*, vol. 32, pp. 510-519, 1961.
- [43] L. Esaki and R. Tsu, "Superlattice and Negative Differential Conductivity in Semiconductors," *IBM Journal of Research and Development*, vol. 14, no. 1, 1970.
- [44] M. Razeghi, *Technology of Quantum Devices*. Springer Science and Business Media, 2010.
- [45] B. Satpati, J. B. Rodriguez, a. Trampert, E. Tournié, a. Joullié, and P. Christol, "Interface analysis of InAs/GaSb superlattice grown by MBE," *Journal of Crystal Growth*, vol. 301–302, pp. 889-892, Apr. 2007.
- [46] C. M. Ciesla et al., "Suppression of auger recombination in arsenic-rich InAs<sub>1-x</sub>Sb<sub>x</sub> strained layer superlattices," *Journal of Applied Physics*, vol. 80, 1996.
- [47] E. R. Youngdale et al., "Auger lifetime enhancement in InAs–Ga<sub>1-x</sub>In<sub>x</sub>Sb superlattices," *Applied Physics Letters*, vol. 64, no. 23, p. 3160, 1994.
- [48] C. H. Grein, P. M. Young, and H. Ehrenreich, "Theoretical performance of InAs/In<sub>x</sub>Ga<sub>1-x</sub>Sb superlattice-based midwave infrared lasers," *Journal of applied physics*, vol. 76, 1994.

- [49] M. E. Flatte, C. H. Grein, J. T. Olesberg, T. C. Hasenberg, and T. F. Boggess, "Temperature dependence of Auger recombination in a multilayer narrow-band-gap superlattice," vol. 58, no. 19, pp. 47-54, 1998.
- [50] S. Maimon and G. W. Wicks, "nBn detector, an infrared detector with reduced dark current and higher operating temperature," *Applied Physics Letters*, vol. 89, no. 15, p. 151109, 2006.
- [51] P. Klipstein et al., "XBn barrier photodetectors based on InAsSb with high operating temperatures," *Optical Engineering*, vol. 50, no. 6, 2011.
- [52] G. C. Dente and M. L. Tilton, "Pseudopotential methods for superlattices: Applications to mid-infrared semiconductor lasers," *Journal of Applied Physics*, vol. 86, no. 3, p. 1420, 1999.
- [53] G. Dente and M. Tilton, "Comparing pseudopotential predictions for InAs/GaSb superlattices," *Physical Review B*, vol. 66, no. 16, p. 165307, Oct. 2002.
- [54] G. C. Dente, M. L. Tilton, a. P. Ongstad, and R. Kaspi, "Wavelength tuning predictions and experiments for type II antimonide lasers," *Journal of Applied Physics*, vol. 103, no. 2, p. 023106, 2008.
- [55] W. M. Rosenow, J. P. Hartnett, and Y. I. Young, *Handbook of Heat Transfer*. 1998, pp. 7.3 - 7.19.
- [56] K. H. Lee and O. C. Kwon, "Studies on a heat-recirculating microemitter for a micro thermophotovoltaic system," *Combust Flame*, pp. 161–172, 2008.
- [57] Y.-heng Li, Y.-sheng Lien, Y.-chin Chao, and D. Dunn-rankin, "Performance of a Mesoscale Liquid TPV Power System," no. December 2008, pp. 327-336, 2009.